PHYSICAL REVIEW B VOLUME 45, NUMBER 12 15 MARCH 1992-II

Two-band model for halogen-bridged mixed-valence transition-metal complexes. II. Electron-electron correlations and quantum phonons

S.M. Weber-Milbrodt
Physikalisches Institut, Universität Bayreuth, W-8580 Bayreuth, Federal Republic of Germany

J. Tinka Gammel
Physikalisches Institut, Universität Bayreuth, W-8580 Bayreuth, Federal Republic of Germany and Centers for Materials Science and Nonlinear Studies and Theoretical Division, Los Alamos National Laboratory, Los Alamos, New Mexico 87545

A.R. Bishop
Centers for Materials Science and Nonlinear Studies and Theoretical Division, Los Alamos National Laboratory, Los Alamos, New Mexico 87545

E. Y. Loh, Jr.
Centers for Materials Science and Nonlinear Studies and Theoretical Division, Los Alamos National Laboratory, Los Alamos, New Mexico 87545 and Thinking Machines Corporation, 245 First Street, Cambridge, Massachusetts 02142-1214

(Received 23 May 1991)

We study the effects of electron-electron interactions in halogen-bridged mixed-valence transition-metal linear-chain complexes (MX chains) applying a simple $\frac{3}{4}$-filled two-band discrete tight-binding (extended) Peierls-Hubbard model with both on-site and intersite electron-phonon couplings. We employ a variety of methods: perturbation theory, Hartree-Fock approximation, and exact diagonalization in the limit of classical adiabatic phonons, and a variational approach allowing for a finite phonon frequency, i.e., quantum phonons and isotope effect. This variety of methods has proven necessary to obtain a complete picture, due to the structural richness of this model. We investigate the competition between the electron-electron and electron-phonon interactions in a wide range of parameter regimes for both ground and excited states. We focus on values relevant to the MX chains, probing the experimental variation as X and M are varied among X=Cl, Br, and I and M=Pt, Pd, and Ni (spanning electron-phonon-interaction-dominated to electron-electron-interaction-dominated materials).

I. INTRODUCTION

As discussed in the companion paper,[1] hereafter referred to as I, there has recently been much interest in halogen-bridged mixed-valence transition-metal linear-chain complexes (MX chains). An introduction to the chemistry of MX materials may be found in the works listed in Ref. 2. Briefly, these materials consist of weakly coupled linear chains of alternating metal (M) and halide (X) atoms. Ligand groups (L) attached to the metals and, in some cases, counterions between chains, complete the three-dimensional (3D) crystalline structure—a typical PtX chain is sketched in Fig. 1. A wide variety of MX chain complexes, with good crystallinity, can be relatively easily synthesized. Related bimetallic (M_2) complexes, and complexes with other bridging groups, are also considered to belong to the "MX class" of materials. For physicists[3] the attraction of the MX chains lies in the fact that they are a class of quasi-1D compounds where the competing electron-phonon and electron-electron interactions vary widely, from the valence-localized limit with strong charge disproportionation of the M sublattice and large structural distortion of the X sublattice (PtCl chains) to the valence-delocalized weakly distorted limit (PtI chains), and also from these charge-density-wave (CDW) phases to the limit where the lattice is undistorted and the M sublattice is believed to have antiferromagnetic (AF) or spin-density-wave (SDW) character (NiBr or NiCl chains). Current synthesis interest lies in exploiting this materials tunability by varying (in order of decreasing magnitude of effect) the metal, the halide, and/or the ligands and counterions, to develop a systematic sequence of materials which span the entire range from strong electron-phonon to strong electron-electron coupling strengths. The synthesis effort is being undertaken in conjunction with a joint experimental and theoretical effort to study the variation of material properties going between these two limits, and especially probing the transition through the highly interesting intermediate coupling region. We strongly feel that this many-fronted "making-modeling-measuring" attack, enabled by the unique materials tunability of the MX class,

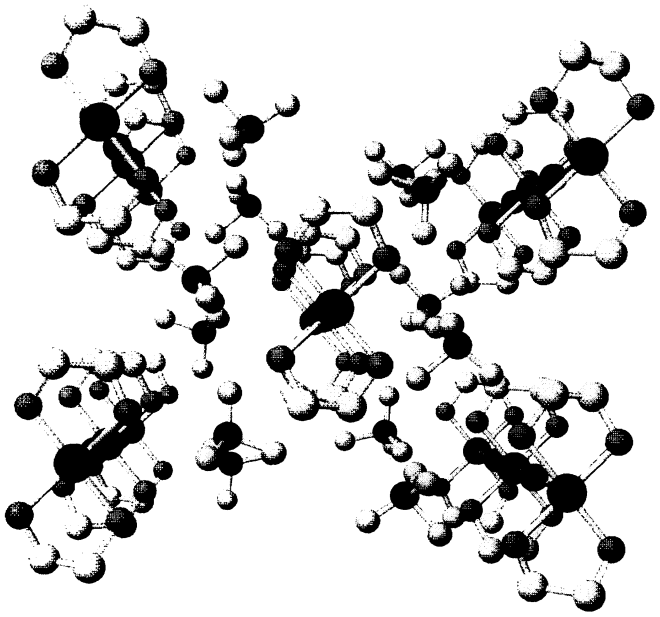

FIG. 1. X-ray diffraction crystal structure of the PtX material $[Pt(en)_2][Pt(en)Cl_2]\cdot(ClO_4)_4$, looking down the chains. There are two equivalent $(ClO_4)^-$ rotations and we have randomly chosen one. The atoms are, from darkest to lightest, Cl, Pt, N, O, and C.

will lead to an enhanced understanding of the competition between the electron-phonon and electron-electron interactions, of fundamental importance to solid state physics, and especially to electronic materials for device applications.

A simple 1D, two-band, discrete, tight-binding Peierls-Hubbard model has proven useful in gaining an understanding of the MX materials.[3] In paper I, we compared this model to previous $\frac{1}{2}$-filled, effective one-band models,[4–8] and discussed the properties of the two-band Hamiltonian in the limit of adiabatic phonons and uncorrelated ($U=0$) electrons. We used tight-binding parameters derived from comparison to band structure[9,10] and *ab initio* quantum chemistry[11] calculations to explain structural, optical, and Raman absorption data on strongly localized materials, where the electron-phonon interaction dominates. One particular success[12] was in obtaining a quantitative fit to the asymmetric electron and hole polaron absorptions of $[Pt(en)_2][Pt(en)_2Cl_2]\cdot(ClO_4)_4$ (en=ethylenediamine). However, since we are interested in understanding the whole MX class and, in particular, the *transition* from electron-phonon interaction dominated materials (e.g., $U \approx t_0$ in PtCl) to electron-electron interaction dominated materials (e.g., $U \approx 3t_0$ in NiBr), the simple $U=0$ adiabatic analysis is incomplete. In this paper we discuss what effects we anticipate due to the inclusion of electron-electron interactions and quantum phonons in the Peierls-Hubbard model for MX chains, which we intend as a guide to help direct the ongoing experimental and synthesis efforts on strongly correlated MX complexes.

Beyond this general hope of gaining a better understanding of competing electron-phonon and electron-electron interactions, the *detailed* discussion here also has a broader relevance, in that the same Peierls-Hubbard model has also been applied to other systems of wide current interest. For instance, the 1D MX class has much in common with current modeling of 2D and 3D oxide superconductors.[13,14] At stoichiometry, both are nominally $\frac{3}{4}$-filled, hybridized two-band materials in which both electron-electron (e-e) and electron-phonon (e-ph) interactions are important — the similarity with $Ba_{1-x}Pb_xBiO_3$ is especially direct.[7,15] This analogy extends to electron or hole *doping* of the broken symmetry ground states leading to discussion of polarons, bipolarons, excitons, and domain walls as self-trapped local defect states (bags), as well as superlattice and spin-Peierls phases. *Asymmetry* between electron and hole polarons, which we find to exist[12] for the MX chains in terms of both the characteristic vibrational modes and the intragap absorption transitions, has been suggested to be of central importance in some recent studies of the quasi-2D oxide superconductors.[16] Clearly, the ability to tune through the transition regions between ground states is especially interesting in this context. In $\frac{3}{4}$-filled two-band models for charge-transfer salts, the Hubbard term is again thought to be very important. Here, strong lattice coupling is also present. An important question for these materials is whether the charge disproportionation is in fact driven by the on-site (β) electron-phonon coupling, or if this is better modeled as being driven by a large Hubbard V term.[17] This same question has also been raised in the context of $Ba_{1-x}Pb_xBiO_3$.[18] In general, it can be shown, e.g., by means of unitary transformations that a β-like electron-phonon coupling term [Eq. (2a) below] gives rise to a contribution to V.[19] This process is related to the well-known creation of a negative Hubbard U by strong on-site electron-phonon coupling.[20] The MX chains have also been modeled by this distance-dependent electron-electron coupling,[21] as opposed to the separation into electron-electron and electron-phonon interactions as done here.

Previous investigations[7] in $\frac{1}{2}$-filled, effective one-band models for the MX materials used the Hartree-Fock (HF) approximation for the electrons (when electronic correlations were included) and the adiabatic approximation for the phonons. However, simple one-band models are problematic even for strongly distorted materials, where naively they should be adequate, as within a one-band ($U=0$ or Hartree-Fock) context the experimentally observed electron/hole asymmetry cannot be easily explained without explicitly invoking additional symmetry-breaking terms. As mentioned above, even with only simple e-ph couplings and no e-e interactions, the two-band model demonstrates an electron/hole asymmetry *quantitatively* in agreement with experiment.[12] As one explores—as is our interest—the trend from strongly localized to more delocalized materials, with decreasing difference in on-site affinities between M and X atoms, effects of the full $\frac{3}{4}$-filled, two-band model are increasingly more important, until finally one passes over to the limit where M and X are degenerate and a "one-band" model is again valid, but with $\frac{3}{4}$ filling (and, in

general, retaining the two different $U_{M,X}$ and $\beta_{M,X}$ values). Further, since fluctuations are usually important in one dimension, it is important to test the validity of adiabatic Hartree-Fock approximation against methods which handle such fluctuations more exactly. Unfortunately, exact quantum many-body methods for studying correlated electron-phonon systems are limited in their ranges of applicability. Quantum Monte Carlo simulations, for example, have provided some results for intermediate strength of electronic correlations and certain doping regimes: however, applications to two bands have proven problematical. An exact treatment of the full quantum-mechanical problem (i.e., numerically exact determination of eigenenergies and eigenstates) exists for very small system sizes only.[22,23]

Thus, to investigate the full two-band tight-binding Peierls-Hubbard Hamiltonian with which we choose to model the MX materials, we apply a variety of different exact and approximate (numerical and analytical) methods to study the effects of electronic correlations and quantum fluctuations of the phonons in order to obtain a more complete qualitative picture, and compare our tight-binding results to *ab initio* quantum chemistry[11] and band-structure[9,10] calculations, which handle the spatial structure of the orbitals, the remaining electrons, and the 3D structure more realistically. The methods we use are (1) a full quantum variational principle (VAQP) described in Appendix A, (2) perturbation theory for small values of the Hubbard parameters (PTCP), (3) completely unrestricted Hartree-Fock approximation (HFCP), and (4) exact diagonalization on small systems (EDCP) described in Appendix B. One class of these approaches (PTCP,HFCP,EDCP) disregards the quantum character of the lattice ("classical" phonons), whereas the other one (VAQP) takes into account the quantum nature of the lattice by explicitly including a finite phonon frequency. Though we focus on the more experimentally relevant adiabatic limit for general parameters, we consider the antiadiabatic limit in addition, where quantum lattice phonon effects dominate, to illuminate the properties of VAQP. We also discuss the zero-hopping ($t_0=\alpha=0$) limit, which gives useful insight into the behavior of strongly distorted (valence localized) MX chains. For weak to intermediate e-e correlations, we find that the three classical treatments agree[24,25] and thus we report here only EDCP and VAQP results for the ground state over a wide range of e-e interaction and quantum lattice phonon fluctuation strengths, and HFCP results for the effects of U on defect absorptions in the adiabatic limit for experimentally relevant parameters.

In Sec. II we describe the model and sketch the various methods we have employed (important technical details can be found in the Appendixes). In Sec. III we discuss parameters appropriate to the MX chains. In Sec. IV we present results for the ground state properties. In Sec. V we report on HFCP calculations for defect states and fits to several specific MX materials. In Sec. VI we summarize our results and the relative advantages of the various approximation schemes for investigating the different material properties.

II. MODEL AND METHODS

Taking into account a single orbital per site (the M d_{z^2} and X p_z orbital) and including only nearest-neighbor interactions (but next-nearest-neighbor effective springs), we use a two-band tight-binding model for an isolated MX chain as in paper I:

$$H = H_{e\text{-ph}} + H_{e\text{-}e} + H_{\text{ph}} , \tag{1}$$

where

$$H_{e\text{-ph}} = \sum_{l,s}\{[-t_0 + \alpha(\hat{x}_{l+1} - \hat{x}_l)]\, c^\dagger_{l+1s} c_{ls} + \text{H.c.}\} + \sum_l [\varepsilon_l - \beta_l(\hat{x}_{l+1} - \hat{x}_{l-1})]\, n_l , \tag{2a}$$

$$H_{e\text{-}e} = \sum_l U_l\, n_{l\uparrow} n_{l\downarrow} + \sum_l V\, n_l n_{l+1} , \tag{2b}$$

$$H_{\text{ph}} = \sum_l \left(\frac{\hat{P}_l^2}{2M_l}\right) + \frac{1}{2}K\sum_l (\hat{x}_{l+1} - \hat{x}_l)^2 + \frac{1}{2}K_{MM}\sum_l (\hat{x}_{2l+2} - \hat{x}_{2l})^2 . \tag{2c}$$

Here $c^\dagger_{ls}$ (c_{ls}) are Fermion creation (destruction) operators describing electrons

$$\{c^\dagger_{ls}, c_{j\sigma}\} = \delta_{lj}\delta_{s\sigma},\ \{c^{(\dagger)}_{ls}, c^{(\dagger)}_{j\sigma}\} = 0,\ n_l \equiv c^\dagger_{l\uparrow}c_{l\uparrow} + c^\dagger_{l\downarrow}c_{l\downarrow},$$

and $\hat{x}_l$ and $\hat{P}_l$ are boson operators describing the vibronic (or oscillatory) degrees of freedom ($[\hat{x}_l, \hat{P}_j] = i\hbar\delta_{l,j}$). We use the convention that M atoms sit on even sites, X atoms on odd sites, and typically employ periodic-boundary conditions, though we have considered boundary-condition dependence. We also typically measure lengths in Å, momenta in sec/cm eV and energies in eV, when not using dimensionless values. The parameters of the model are the electron hopping integral between adjacent M and X sites (t_0), the difference between metal and halogen electron affinities ($\varepsilon_l = [\varepsilon_X = -e_0, \varepsilon_M = +e_0]$), an on-site ($\beta_l = [\beta_X, \beta_M]$) and intersite ($\alpha$) electron-phonon coupling, on-site ($U_l = [U_X, U_M]$) and intersite (V) electron-electron repulsion, the masses of the M and X atoms ($M_l = [M_X, M_M]$), and finally effective metal-halogen (K) and metal-metal (K_{MM}) springs which model the elements of the structure not explicitly included, such as the core electron repulsion and the ligand-ligand interaction. The model parameters are shown schematically in Fig. 2 of I. At stoichiometry there are three electrons per MX unit—i.e., $\frac{3}{4}$ filling.

At this point we have not included second-neighbor terms or longer-range Coulomb interactions in the Hamiltonian as we do not believe they are qualitatively important (based on preliminary investigation[26] of the effects of such terms), although they may be necessary for detailed

quantitative fits to experiment on a given material, particularly one with strong disproportionation, e.g., PtCl.[27]

Equilibrium displacements from uniform lattice spacing are given by $\Delta_l = \langle \hat{x}_{l+1} - \hat{x}_l \rangle$. Within the adiabatic approaches, the self-consistent lattice distortion is found iteratively from

$$0 = (\delta H_{e\text{-ph}}/\delta\Delta_\ell)(\Delta_n^{\text{old}}) + (\delta H_{\text{ph}}/\delta\Delta_\ell)(\Delta_n^{\text{new}}) \ . \tag{3}$$

Defect configurations are calculated by adding or subtracting electrons from a neutral chain of length $4N$ (or $4N+2$ for solitons) and adiabatically relaxing the lattice to the new ground state. Optical-absorption spectra are calculated from the Fermi golden rule

$$\alpha(\omega) = \frac{\pi}{\omega} \sum_{f,i} |\langle f|J|i\rangle|^2 \delta(\omega - e_f + e_i) \ , \tag{4}$$

where f, i denotes the final and initial states and

$$J = i \sum_{\ell,\sigma} (-t_0 + \alpha\Delta_\ell)(c^\dagger_{\ell\sigma} c_{\ell+1\sigma} - c^\dagger_{\ell+1\sigma} c_{\ell\sigma}) \ , \tag{5}$$

and Lorentzian broadened. HFCP calculations were typically done on lattices of 100 sites, though for the more delocalized materials lattices of up to 400 sites were used as needed to remove most of the artificial oscillations in the spectra introduced by this procedure.

The details of the VAQP and EDCP approaches to solve the above Hamiltonian are very interesting but mainly technical, therefore they are summarized in Appendixes A and B, respectively. Note that EDCP can be viewed as a variational treatment, and thus comparison of energies obtained using EDCP and VAQP methods (with the zero-point energy subtracted) is a measure of the importance of correctly treating e-e correlations and ignoring the quantum nature of the phonons vs mapping e-e correlations to e-ph coupling terms and including quantum lattice phonons. In order to facilitate this comparison with EDCP, we have limited the VAQP to small system sizes, though the VAQP can, in general, be solved numerically on quite large system sizes. The PTCP, where e-e interactions are treated in second-order perturbation theory, is a standard technique, and we do not describe it further here. HFCP, where the many-body terms are replaced with the averages based on Wick's theorem, while also fairly standard, we review in Appendix C for the purposes of definiteness. For small to intermediate U, we find agreement of EDCP and HFCP calculations to be excellent (for both ground and defect state structure and optical absorption). This is a consequence of the $\frac{3}{4}$ filling in a CDW regime and is to be contrasted with the $\frac{1}{2}$-filled one-band case, where it is well known that e-e correlations are not adequately described in HF approximation. Because of the agreement between HFCP and EDCP, we expect the trends discussed in paper I to hold equally well for small to intermediate U. For a given set of parameters with $U \neq 0$, within HF approximation one can define HF effective $U = 0$ parameters which give the identical ground-state band structure and charge densities as the parameters with $U \neq 0$. This mapping of parameters is given in Table I. Note however, the defect absorptions and lattice dynamics predicted within HFCP for finite U do *not* agree with the predictions from the HF effective $U = 0$ parameters, as discussed below. Also listed in Table I are the effective one-band parameters,[28] for easier comparison to previous work within the one-band scheme,[7] and our definition of dimensionless parameters, important to remove the trivial scalings for parameter space investigation.

III. DETERMINATION OF PARAMETERS FOR MX CHAINS

In the spirit of our "making-modeling-measuring" attack, we have attempted to determine parameters for the MX materials from comparison with band-structure calculations[9,10] in local-density approximation with self-interaction correction (LDA-SIC) appropriate for more delocalized materials, and *ab initio* quantum chemistry calculations[11] on small clusters (including ligands) appropriate to the highly valence localized limit, with minimal input from ground-state experimental data (such as the measured lattice distortion amplitude). These calculations were performed at the experimental geometry as well as nearby geometries to allow determination of the distance dependent (electron-phonon) and independent (single electron and electron-electron) tight-binding parameters in Eq. (1). The effective M-X spring constant was then determined by requiring these parameters to satisfy the self-consistency condition Eq. (3). We further checked that the predicted ground-state properties

TABLE I. (a) Model parameters, (b) the corresponding dimensionless parameters, (c) the effective one-band parameters for large e_0 (Ref. 28), and (d) the effective U=0 parameters that give the same band structure as the bare parameters with U, assuming a CDW. Here $\rho_{M(X)}$ is the average charge on the $M(X)$ sites, and $2\delta\rho_M$ is the difference in charge of the inequivalent metal atoms. Note that the entire two-band phase diagram for positive β and e_0 maps into only the CDW part of the one-band phase diagram, but U can cause a negative β, reintroducing the BOW phase.

(a)	H	t_0	α	e_0	β	K	Δ
(b)	$\frac{H}{2t_0}$	$\frac{t_0}{2t_0}$	$\frac{\alpha}{2\alpha}$	$\frac{e_0}{2t_0}$	$\frac{\beta}{2\alpha}$	$\frac{Kt_0}{2\alpha^2}$	$\frac{\alpha\Delta}{t_0}$
(c)	H	$\frac{t_0^2}{2e_0}$	$\frac{\alpha t_0}{2e_0}$	(∞)	$\beta + \frac{\alpha t_0}{e_0}$	K	Δ
(d)	$H + \langle\hat{U}\rangle$	t_0	α	$e_0 + \frac{U_M\rho_M - U_X\rho_X}{4}$	$\beta_M - \frac{U_M\delta\rho_M}{4\Delta}$	$K - \frac{U_M\delta\rho_M^2}{4\Delta^2}$	Δ

TABLE II. Parameters for the Pt materials from comparison to *ab initio* calculations (Ref. 11). These numbers are scaled to match ground-state experimental data (optical gap, lattice distortion amplitude) on PtCl (Refs. 3 and 12), as the IVO (improved virtual orbital) corrections to the *ab initio* calculations are still in progress. These numbers are to be interpreted as effective $U = 0$ mean-field values. The difference in the two sets is most likely due to the neglected Hubbard U reducing β.

MX	$e_0/2t_0$	$\beta_M/2\alpha$	$Kt_0/2\alpha^2$	$\alpha\Delta/t_0$	$E_g/2t_0$	Δ (Å)	E_g (eV)
From comparison to *ab initio* without IVO, K, and gap energy E_g calculated							
PtCl	0.27	0.16	1.59	0.15	0.27	0.38	2.5
PtBr	0.19	0.17	1.84	0.11	0.20	0.29	1.9
PtI	0.10	0.20	2.40	0.06	0.12	0.18	1.1
Scaled to experiment on PtCl (Ref. 12)							
PtCl	0.3	0.030	0.52	0.6	0.81	0.38	2.5
PtBr	0.2	0.035	0.69	0.4	0.58	0.24	1.5
PtI	0.1	0.040	1.02	0.2	0.30	0.14	1.2

such as the optical gap and band widths and separation between M and X bands agreed with the experimental inter-valence-charge transfer (IVCT) band edge and width and the $\sigma(\mathrm{Cl}) \rightarrow d\sigma^*$ absorption for the oxidized monomer in solution (or the difference in electron affinities of the constituent M and X), respectively, to the extent that these have been measured. In cases where the theoretical calculations have not been performed, we also used these experimental ground-state data to help determine parameters.

Our current best estimates are shown in Tables II and III. Note that for CDW materials, this parametrization is insensitive to K_{MM} and β_X. The success of these parameters is judged by how well other material properties are predicted, both ground state, such as the ir and Raman-active phonon modes, and excited state, such as the location of intragap absorptions due to electron and hole polarons, again to the extent that these have been measured. As discussed in paper I, the predicted optical absorptions for $U = 0$ are relatively insensitive to exact parameters for $K_{MM} \gtrsim K$, with the degree of distortion ($\alpha\Delta/t$) apparently being the controlling factor in determining the spectra. Thus, for simplicity, we use $K_{MM}=\infty$ when phonon frequencies are not explicitly considered. We find roughly a "factor-of-2" agreement between parameters determined by different theoretical schemes and the parameters chosen to best fit experiment, which we feel at this stage is encouraging. In paper I, we discuss how these fits lead to the HF effective $U = 0$ parameters modeling PtCl: $t_0 = 1.6$ eV, $\alpha = 2.4$ eV/Å, $e_0 = 0.96$ eV, $\beta_M = 0.16$ eV/Å, and $K = 3.9$ eV/Å^2. In dimensionless notation (see Table I), this corresponds to $t_0 = 0.5$, $\alpha = 0.5$, $e_0 = 0.3$, $\beta = 0.03$, $K = 0.5$, and $\Delta = 0.6$. Since the HF scaling back to the bare parameters increases β and K, to investigate the U dependence of a "typical" strongly distorted material, we have also used the following parameter set: $t_0 = 0.5$, $\alpha = 0.5$, $e_0 = 0.6$, $\beta = 0.3$, $K = 1.0$, and $\Delta = 0.5$. In general, for the Pt materials, we expect the Hubbard U to be in the range 1–2 eV.[10] For the Pd materials, we expect only e_0 to decrease. Finally, for the Ni materials, we expect roughly $t_{\mathrm{Ni}} \sim \frac{1}{2}t_{\mathrm{Pt}}$, $e_{\mathrm{Ni}} \sim 0$, and $U_{\mathrm{Ni}} \sim 3t_{\mathrm{Ni}}$.[10] The expected trends for α and β are *a priori* unclear, and, until the band structure and *ab initio* calculations are complete, we use the Pt values, scaled as t_0 scales ($\alpha_{\mathrm{Ni}} \simeq \alpha_{\mathrm{Pt}} t_{\mathrm{Ni}}/t_{\mathrm{Pt}}$). We note for the Ni$X$ parameters

TABLE III. Parameters from comparison to band-structure calculations (Refs. 9 and 10) on Ni materials. The method used to extract the Hubbard U from the SIC-LDA calculations is the same as used for the oxide superconductors (Ref. 10). The values for α, β, and K were taken from the corresponding Pt material, scaled as t_0 scales. The effective PtCl and PtBr parameters (arbitrarily) adjusted to $U_M = t_0/2$, are included for ease of comparison. The optical gap is the experimental value (Ref. 29), and does not agree with the gap calculated in HFCP (see text).

MX	E_g (eV)	Δ_0 (Å)	t_0 (eV)	α (eV/Å)	e_0 (eV)	β_M (eV/Å)	K_{MX} (eV/Å^2)	U_M (eV)	U_X (eV)
PtCl	2.5	0.38	1.54	2.38	0.66	0.44	4.4	0.77	
PtBr	1.5	0.24	1.30	2.17	0.29	0.49	5.7	0.65	
PtI	1.2	0.15	1.99	2.65	0.04	0.78	8.5	1.00	
NiCl	1.9	0	1.05	1.62	0.48	1.19	5.6	2.7	1.6
NiBr	1.3	0	0.95	1.59	0.51	1.52	7.9	2.6	1.1

listed in Table III, that the predicted optical gaps within HFCP do *not* agree with the experimentally reported values listed in the table.[29] Comparison with EDCP also indicates the HFCP gap is a factor of 2 too large even if the parameters were correct. For the listed values of U_M and U_X, it is difficult to obtain a larger gap for NiCl for roughly equal values of e_0 as is indicated by the band-structure calculation. Without further theoretical guidance, and since some open questions remain in the interpretation of the experimental spectra, we feel it best to consider the parameters listed as representative values.

More detailed parameter determination is underway,[30] including calculation of vibrational information (e.g., LO phonon-mode frequency) to compare with infrared and Raman data. Of course, the Raman-active X-X stretch will also be insensitive to K_{MM} and β_X. The exact values of these parameters are however important in the ground state when calculating the (ir active) modes involving movement of the metal atoms:

$$M \rightarrow\leftarrow X\ M \rightarrow\leftarrow X \text{ and } M \rightarrow X \leftarrow M\ X\ .$$

We fully expect the numbers in Tables II and III to change as the *ab initio* and band-structure calculations are refined. In particular, the IVO (improved virtual orbital) corrections, which correct excited states for e-e correlations, were not included in the *ab initio* calculations we compare to here, and the band-structure calculations have not yet been done on the Pd materials or chains with non-neutral ligands. Further, a 1D band-structure technique[31] is under development which incorporates some *ab initio* features and which should be more reliable for these quasi-1D materials.

IV. GROUND-STATE PROPERTIES

We have studied the effects of including electron-electron correlations on the ground-state lattice distortion in both the antiadiabatic limit, where the quantum nature of the lattice phonons dominates, and in the more experimentally relevant adiabatic limit where the quantum nature of the lattice can be ignored. We also discuss the zero-hopping limit ($t_0 = \alpha = 0$), which gives useful insight into the behavior of those MX chains which fall into the strongly distorted, valence-localized regime. In the following discussion of the ground states we have also set $K_{MM} = 0$, as we are interested in exploring the possibility of ground-state phases [e.g., BOW (bond-order wave), long-period] besides the (experimentally observed) commensurate period four CDW and SDW or AF ground-state phases, on which the value of K_{MM} has no effect. (As noted above, the value of the metal-metal spring is very important when considering excitations from these phases, or certain ir active phonon modes.) The ground-state phase diagram in the absence of electron-electron correlations and quantum phonon fluctuations was discussed in paper I. Note that, in our notation, CDW, SDW, and BOW refer to the M atoms. In the CDW (BOW) phase, the X atoms exhibit a BOW (CDW). The antiferromagnetic (AF) phase is found only in EDCP, and corresponds to the "mean-field" SDW phase found by the other techniques; for purposes of general discussion we take "SDW" to mean both, though of course a *truly* 1D system cannot exhibit a full broken-symmetry SDW. Further, strong antiferromagnetic correlations can exist[32] in both the CDW and BOW phases, and these might be better interpreted as "spin-Peierls" phases[33] in a generalized sense.

A. Antiadiabatic limit

Though the limit of large phonon frequencies is not relevant for the description of current experimental results on MX complexes, it helps to illuminate very general aspects of our model and methods, especially the VAQP — relevant for other materials and perhaps also in transition regions for MX chains.

1. Zero mass

To gain insight into the interplay between electron-phonon and electron-electron interaction, we examine the partition function of our model

$$Z = \mathrm{Tr}\ \exp(-\beta H)\ . \tag{6}$$

The trace over the phonon part may be written as a path integral. In the (unphysical) limit of zero masses of the M and X atoms, we have for Z

$$Z = \mathrm{Tr} \int \mathcal{D}[\delta_1(\tau)] \cdots \mathcal{D}[\delta_N(\tau)] \exp\left\{ - \int_0^\beta d\tau \left[\sum_l \left(\frac{K}{2} \delta_l^2(\tau) + \delta_l(\tau) I_l \right) + H_e \right] \right\}\ , \tag{7}$$

where H_e denotes the pure electronic part of the Hamiltonian and I_l is given by

$$I_l = \alpha B_{l,l+1} - (\beta_l n_l + \beta_{l+1} n_{l+1}) \tag{8}$$

with

$$B_{l,l+1} = \sum_s \left(c_{l+1s}^\dagger c_{ls} + \mathrm{H.c.} \right)\ . \tag{9}$$

In this case the phonon degrees of freedom may be integrated out to yield an effective electronic contribution to Z

$$Z_e = \mathrm{Tr} \exp\left[-\beta \left(H_e - \frac{1}{2K} \sum_l I_l^2 \right) \right]\ . \tag{10}$$

Interpreting this result as defining an effective Hamiltonian for the electronic degrees of freedom, we see that it possesses both renormalized electronic model parameters

$$U_l^{\mathrm{eff}} = U_l - \frac{2}{K} \beta_l^2, \tag{11a}$$

$$V_l^{\mathrm{eff}} = V - \frac{1}{K} \beta_l \beta_{l+1}, \tag{11b}$$

$$\varepsilon_l^{\text{eff}} = (-1)^l e_0 - \frac{1}{K}\beta_l^2, \tag{11c}$$

and additional types of electronic interaction terms acting like an attractive bond-bond interaction,

$$H_W^{\text{int}} = -\frac{\alpha^2}{2K}\sum_l B_{l,l+1}^2, \tag{11d}$$

and a density dependent hopping that breaks the particle hole symmetry,

$$H_X^{\text{int}} = \frac{\alpha}{2K}\sum_l [\, B_{l,l+1}(\beta_l n_l + \beta_{l+1} n_{l+1}) + (\beta_l n_l + \beta_{l+1} n_{l+1}) B_{l,l+1}] \,. \tag{11e}$$

Summarizing, we see that in this antiadiabatic regime the off-diagonal electron-phonon interaction (modeled by α) is responsible for an attractive electronic bond-bond interaction H_W^{int} and (in conjunction with β_l) for a modified so-called "X term," H_X^{int}.[34] The latter result might be of general importance in a 2D version of our model for the mediation of superconducting pairing by a Coulomb interaction between an atomic charge and a bond charge formed by the overlap of two orbitals on neighboring sites (compare Ref. 35, where a phononless two-band model is treated).

The renormalization of the electronic parameters is intriguing, since it could lead to bipolaronic pairing depending on the strength of the e-ph coupling parameters.[36] The on-site electron-phonon coupling (modeled by β_l) mimics an attractive (negative) Hubbard U, and a Hubbard V. The additional V term in Eq. (11b) is always attractive for site-independent β_l. In case of a large staggered β [$\beta_l \propto (-1)^l$], a repulsive V^{eff} is combined with an attractive U^{eff}. Note that processes creating an effective negative U (e.g., strong electron-phonon coupling or nonlinear screening in combination with intrinsic electronic properties, respectively) have been proposed for driving electron pairing in the oxide superconductors.[18,20] Finally, we see that the ionization potential ε_l is lowered by β_l, independent of the sign of β_l.

2. *Small but finite mass*

To study the antiadiabatic limit (limit of large ω^* where ω^* is the phonon frequency defined in Appendix A) using the VAQP approach described in Appendix A, we measure all energies in units of $\hbar\omega^*$. For our model calculations we use the following scaled parameters: $t_0' = t_0/(\hbar\omega^*)$, $\alpha' = \alpha(\hbar\omega^* 4f^*)^{-1/2}$, $\beta' = \beta(\hbar\omega^* 4f^*)^{-1/2}$, $K' = K/(4f^*)$, $U_l' = U/(\hbar\omega^*)$, $\varepsilon_l' = (-1)^l e_0/(\hbar\omega^*)$. Fixing $t_0 = 0.5$ in these units, taking into account the experimental value of 3.1 eV for t_0, and recalling from Appendix A that $\omega^{*2} = f^*/m^*$, if the scaling force constant f^* is chosen to be 4.8 eV/Å^2, then the effective mass $m^*=2M_M M_X/(M_M + M_X)$ approximately equals the mass of an electron.

Figure 2 shows the upper bound to the true (quantum) ground-state energy per lattice site obtained by EDCP (dash-dotted) and by the VAQP (solid) for two values of site-independent β, using equal M and X masses in this antiadiabatic limit. The zero-point energy was subtracted. Note that the EDCP variational results do not depend on the mass ratio of M and X atoms. We found that for small values of U, the VAQP always yields a lower bound than the EDCP, i.e., the VAQP gives a quantum gain in this region. For fixed t_0, α, and small β, the point where the two curves intersect moves to higher values of U with increasing ionization potential e_0, indicating that the quality of the VAQP, compared to the EDCP bound, increases with e_0. In addition, the relative distance between the two bounds decreases with increasing e_0, as can be seen by a comparison of the curve pairs (a) and (b) in Fig. 2. For reasonably small values of the Hubbard U, a CDW state exists with decreasing amplitude as a function of increasing U. In Fig. 3(a), the CDW amplitudes obtained by HFCP, PTCP, and EDCP (adiabatic cases) are compared to the antiadiabatic limit obtained by VAQP for 12 lattice sites. The reduction of the VAQP-CDW amplitude even at $U = 0$—with respect to the other approaches—is due to the large phonon frequency. Figure 3(b) shows the corresponding absolute quantum gain of VAQP compared to EDCP ($\Delta E'$), i.e., the difference of both energy bounds. This difference is positive for $0 < U' < 2$ and shows a maximum near $U' = 0.5$ and goes to 0^- for growing intermediate U' indicating the relevance of quantum effects within our VAQP for small and intermediate values of U' only. Since the absolute quantum gain $\Delta E'$ depends on the actual size of the energies and hence on scaling, the relative quantum gain Q is plotted in Fig. 3(c) (defined as $\Delta E'$ divided by the mean value of the corresponding energies). The conclusions obtained from Fig. 3(b) are equally valid. Figure 4 shows the system size dependence of the CDW amplitude Δ obtained by VAQP. (Larger system sizes are accessible using VAQP, but we restrict ourselves here to sizes accessible by EDCP to facilitate comparison.) The drop of the CDW amplitude to zero steepens with increasing sys-

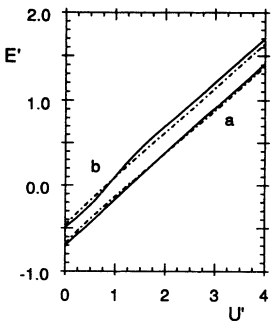

FIG. 2. The upper bound to the true (quantum) ground-state energy per lattice site as a function of Hubbard U, obtained by EDCP (solid) and by the quantum phonon variational approach (VAQP), (dash-dotted), using equal M and X masses in the antiadiabatic limit. The curves shown are for an eight-site system with $\tilde{t}_0 = 0.5$, $\tilde{\alpha} = 0.5$, $\tilde{K} = 1.0$, $\tilde{K}_{MM} = 0.$, $\tilde{\beta} = 0.1$, and $\tilde{e}_0 = 1.0$ (curve pair a) and $\tilde{e}_0 = 0.1$ (curve pair b). The zero-point energy E_0 was subtracted.

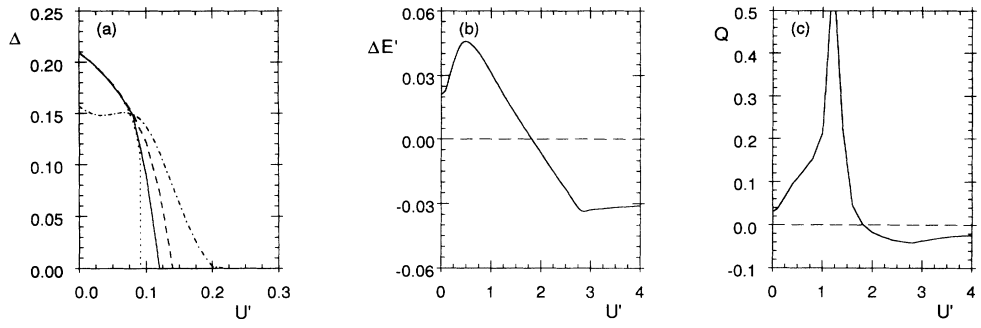

FIG. 3. Comparison between our different approaches for a 12-site system and the same parameters as curve *a* of Fig. 2. (a) The (antiadiabatic) CDW-state amplitude Δ as a function of Hubbard U using (1) VAQP for equal masses (dash-dotted), (2) EDCP (solid), (3) HFCP (dashed). and (4) PTCP (dotted). (b) The quantum gain of VAQP with respect to EDCP (defined as the difference of the corresponding energy bounds) for $0 < U' < 4$. (c) The relative quantum gain of VAQP with respect to EDCP (defined as the difference of the corresponding energy bounds divided by their mean value).

tem size. In addition the absolute value of Δ is sensitive to Jahn-Teller and non-Jahn-Teller systems, i.e., $8n$ and $8n + 4$ site systems, since periodic-boundary conditions were employed, as is familiar from HFCP calculations on small systems.

For small masses in the parameter regime under consideration, the influence of quantum fluctuations contained in the VAQP removes the BOW phase, found in our adiabatic treatment, and the CDW phase goes directly into a SDW phase of zero distortion as U increases. The loss of the BOW phase through quantum fluctuations is interesting, since there exist experimentally no compounds where a BOW phase is reported, although a possibly SDW or AF phase has been observed (e.g., NiBr). At larger U, a CDW/spin-Peierls phase again occurs. This reentrant lattice dimerization is also found in Hartree-Fock[24] but at much larger U.

Since the VAQP allows for different phonon frequencies, we also investigated varying the mass ratio at fixed m^*. In the following discussion we use $\sigma_0 = m^*/M_X$ to describe varying mass ratios. Its relation to M_M/M_X is shown in Fig. 5. Using $t_0' = 0.5$, $\alpha' = 0.5$, $e_0' = 1.0$, $\beta' = 0.1$, and $K' = 1.0$, our results indicate that for $N = 8$ and small values of U' the CDW state has the lowest energy as in the case of equal masses. Figure 6 demonstrates the dependence of total energy per lattice site on σ_0 for U'=0 and 8- and 12-site lattices. We see that for the isotope effect at constant reduced mass in absence of electronic correlations, largely different mass ratios lower the total energy compared to the case of equal masses. As expected from the well-known Jahn-Teller versus non-Jahn-Teller behavior, the $N = 12$ site system is lower in energy. Figure 7 shows the total energy per lattice site for $U' = 0.1$ and 16 lattice sites as a function of σ_0. This function is more symmetric with respect to its maximum than in the uncorrelated case. The CDW-displacement amplitude also varies with the mass ratio: see Fig. 8, where the Δ dependence on σ_0 is shown for the same parameters as in Fig. 6. At $U' = 0$ the maximum of the CDW amplitude is found for M_M slightly smaller than M_X. Generally, for very different M_M and M_X the CDW distortion is smaller than for nearly equal masses. Thus, for a large ratio $M_M : M_X$, the CDW amplitude is significantly smaller than at the maximum, and decreases as this ratio increases. The SDW phase exists in a wider Hubbard U interval for unequal masses than it does for equal masses. For $M_M : M_X = 9$, the onset of the spin-Peierls phase is near $U = 8t_0$, whereas for equal masses, it is found to be near U=$6t_0$ and U'=0.1.

B. Zero-hopping limit ($t_0 = \alpha = 0$)

1. Adiabatic zero-hopping limit

The adiabatic zero-hopping, or atomic, limit provides useful insight into our model when quantum phonon ef-

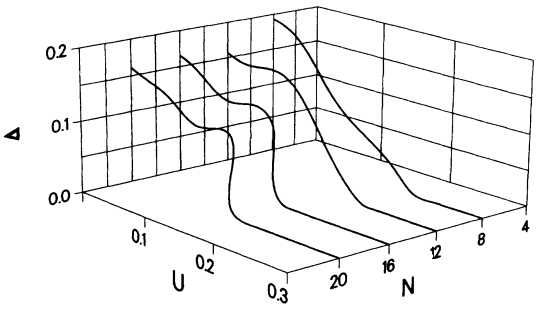

FIG. 4. CDW-state amplitude as a function of Hubbard U and system size (N=8,12,16,20) in the VAQP approach for the parameters of Fig. 3.

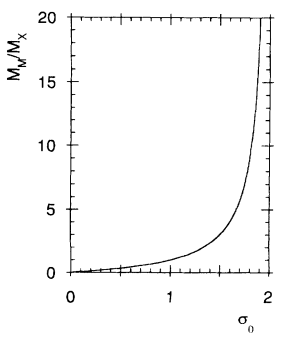

FIG. 5. The relation of the real mass ratio M_M/M_X and σ_0 (see text).

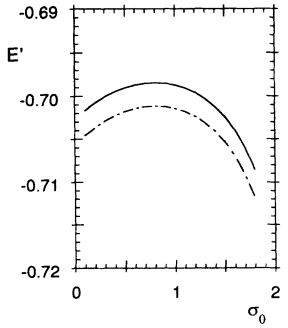

FIG. 6. The total VAQP energy per lattice site as a function of σ_0 for $U = 0$ and $N = 8$ (solid), $N = 12$ (dash-dotted). Other parameters are $t_0' = 0.5$, $\alpha' = 0.5$, $e_0' = 0.1$, $\beta' = 0.1$, $K' = 1.0$, $K'_{MM} = 0$ (same parameters as curve b of Fig. 2).

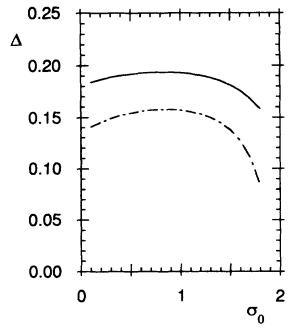

FIG. 8. The VAQP CDW-displacement amplitude Δ as a function of σ_0 for $N = 12$, and $U = 0.0$ (solid), $U = 0.1$ (dash-dotted). Other parameters as in Fig. 6.

fects can be ignored and the material is in the strongly-distorted valence-trapped regime, as is the case for PtCl. Again, for the discussion here, we have set the metal-metal spring to zero to investigate most generally the possibility of other phases. The competition (see above discussion of the antiadiabatic limit) between the on-site electron-phonon coupling (β) and the Hubbard terms (U, V) remains:

$$H_{\text{zero}} = \sum_l [\varepsilon_l - \beta_l(\Delta_l + \Delta_{l-1})]\, n_l + \sum_l U_l\, n_{l\uparrow} n_{l\downarrow} + \sum_l V\, n_l n_{l+1} + \frac{1}{2} K \sum_l \Delta_l^2 \,. \tag{1'}$$

The Hamiltonian is now site-diagonal, and may be easily minimized, yielding the following phases.

a. Period 4. While *a priori* there is no reason to rule out the existence of nonperiod 4 ground states, we first constrain the ground state solution to be period 4 or lower. This, of course, includes the possibility of a phase of no distortion. This situation is easily investigated in the zero-hopping limit, as the eigenstates are fully described by the occupancy of the Wannier orbital at each site. The possible period-4 phases for $V = 0$ are listed in Table IV. We have used both MACSYMA and MATHEMATICA to investigate the phase diagram,[25] shown in Fig. 9. We find that at fixed β_X^2/Ke_0 and β_M^2/Ke_0, for small to intermediate values of U_M and U_X the CDW phase is favored, in agreement with the observed behavior of the majority of the known MX materials.[2] For larger values of U_M or U_X the system is undistorted and shows antiferromagnetic behavior on the M (MAF) or X (XAF) sublattices, respectively ($XMXM \cdots = \uparrow\downarrow\ \downarrow\ \uparrow\downarrow\ \uparrow \cdots$ or $\downarrow\ \uparrow\downarrow\ \uparrow\ \uparrow\downarrow \cdots$), in agreement with the recent synthesis of undistorted, antiferromagnetic MX materials.[37,38] For small U_X, the transition from the CDW to the undistorted phase takes place at $U_M = 2\beta_M^2/K$.[7] The ground state is a BOW for negative values of U_M only. (Reversing the sign of e_0 interchanges the roles, or definitions, of the CDW and the BOW phases.) Note that, since $U_M \geq 0$, the two-band model predicts that the BOW phase will not be observed, in agreement with the lack of observation of BOW MX materials.[2] This is to be contrasted with effective $\frac{1}{2}$-filled one-band models,[7] where the BOW phase would be expected to occupy a substantial portion of the phase diagram (if one-band parameters are *not* derived from the two-band model), which thus cannot explain the experimental lack of BOW phase materials.

b. Long period. While Peierls's theorem[39] guarantees that a commensurate distortion is lower in energy than no distortion in 1D electron-phonon coupled systems, it does not exclude the possibility that an incommensurate distortion will be *even* lower in energy. Interestingly, for

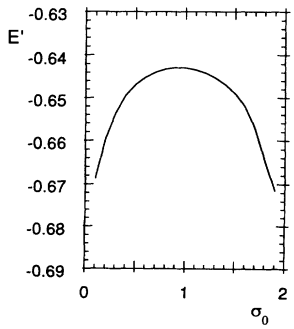

FIG. 7. Same as Fig. 6, but for $U = 0.1$ and a 16-site system.

TABLE IV. The charge configurations in real space and energies of the period-4 phases in the zero-hopping limit for $V = 0$. Here $u_{m,x} = U_{M,X}/e_0$ and $b_{m,x} = (\beta_{M,X})^2/(Ke_0)$. The unpaired electron may have either spin up or down, but for nonzero t_0, the corresponding 1D antiferromagnetic phase (SDW in HFCP) is found.

	$XMXM$	$2E_4/(e_0 N)$
MAF	2 1 2 1	$u_x - 1$
XAF	1 2 1 2	$u_m + 1$
CDW	2 2 2 0	$u_x - 1 + u_m/2 - b_m$
BOW	2 2 0 2	$u_m + 1 + u_x/2 - b_x$
MIX	2 2 1 1	$u_x/2 - b_x/4 + u_m/2 - b_m/4$

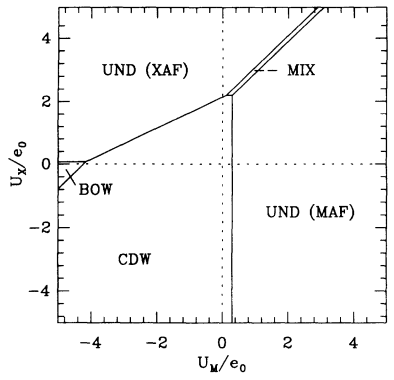

FIG. 9. $K_{MM}=0$ ground-state phase diagram in zero-hopping limit for $\beta_M^2/Ke_0=0.15$, $\beta_X=-\frac{1}{2}\beta_M$.

our model, Eq. (1), we find that the on-site electron-phonon coupling β can drive long-period ground states even at *exactly* commensurate filling.

Recall in the zero-hopping limit the period-4 CDW phase is, in site-occupancy notation:

$$\cdots XMXMXMXM\cdots = \cdots 20220220220\cdots .$$

For $U=0$ and $\beta_M=\beta_X=\beta$, it is easily seen that the lowest energy state for small e_0 phase separates into two regions, one of which has all the sites fully occupied and one of which has all the sites empty:

$$222\cdots 2220\cdots 0 .$$

This is to be expected from the antiadiabatic (Sec. IV A 1) and mean-field (Sec. IV C 2) predictions that β acts like a negative Hubbard U. However, hopping and long-range Coulomb effects clearly disfavor such a "clumped" phase. In Ref. 40 we investigate the possibility of long-period phases in the presence of an unscreened Coulomb interaction plus an on-site exchange, treating the hopping t_0 in perturbation theory. Our analysis there for small t_0 and fixed strength of the electron-electron correlations at $\frac{3}{4}$ filling shows that, as β is increased, there is a sequence of transitions through the states C_1, C_3, C_5, ..., C'_α, $C'_{\alpha+1}$, ..., C'_∞, where we have defined the $\frac{3}{4}$-filled period 4α states C_α:

$$\underbrace{2\,2\,2\,\cdots\cdots\,2\,2\,2}_{3\alpha\text{ sites}}\ \underbrace{0\cdots 0}_{\alpha\text{ sites}} ,$$

and C'_α:

$$\underbrace{2\,2\,\cdots\cdots\,2\,2}_{2\alpha\text{ sites}}\ \underbrace{1\,1\,\cdots\cdots\,1\,1}_{2\alpha\text{ sites}} .$$

We regard this tendency as the manifestation of an 1D analog of twinning. The "charge-clumping"—the effective attraction between sites and regions with real-space double occupancy of the electronic levels — can also be interpreted as pairing of "bipolarons" in 1D. The extent to which these effects (twinning and "bipolaronic pairing"[41]) persist in a 2D extension of our model has not been investigated. Because this intriguing phenomenon is discussed in detail in Ref. 40, we limit the discussion in the rest of this paper to ground-state solutions of period 4 or lower, including the possibility of a phase of no distortion, and localized defects with respect to such ground states.

2. *Quantum phonon zero-hopping limit*

The VAQP approach is also able to handle the zero-hopping limit. Using the unscaled parameter set of Sec. IV C below ($0 < U < 25$ eV), we find that for finite masses the CDW phase is numerically unstable at $U=0$. Instead, the system is in a phase of no distortion (quantum melting). The energy is found to be independent of the total mass (m^*), and numerically identical to the energy of the classical zero-hopping undistorted phase (up to zero-point energy). Figure 10 shows the energy of this phase of no distortion obtained by VAQP in comparison with the energy of the classical zero-hopping CDW configuration, obtained in Sec. IV B 1 a above. Again the zero-point energy has been subtracted from the VAQP results. A similar behavior was found for other parameter sets (not relevant for the MX class of materials under consideration) too.

C. Typical parameters for MX chains

1. *Quantum phonons and electron-electron correlations*

We now use the VAQP and EDCP methods to study the relative importance of quantum phonon and electron-electron correlation effects for *realistic* model parameters. We limit ourselves to short lattices (mostly $N=8$) to allow a comparison with EDCP. Note that, similar to HFCP, the VAQP is able to treat a much greater number of lattice sites but is only an approximate treatment for e-e correlations. In Sec. IV A 2 above, we varied the mass ratio at fixed total mass m^*. Now we

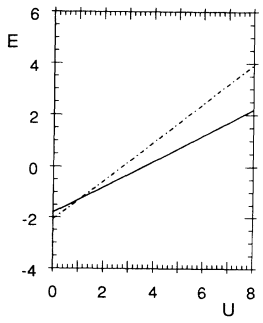

FIG. 10. Quantum phonon zero-hopping limit. Shown is the VAQP bound for the ground-state energy (solid), the energy of the classical adiabatic CDW (dash-dotted), and the energy of the undistorted (solid) states as a function of U. All energies are measured in eV, and the parameters are $t_0=\alpha=0$, $e_0=3.6$ eV, $\tilde{\beta}_M=0.16$ eV/Å, $\tilde{\beta}_X=-0.8$ eV Å, $K=4.8$ eV/Å^2, and $K_{MM}=0$.

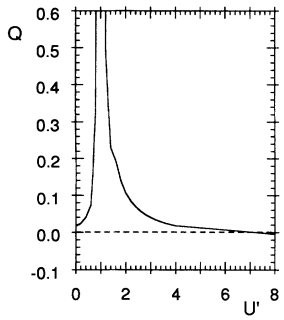

FIG. 11. The relative quantum gain of VAQP with respect to EDCP [defined as in Fig. 3(c) for $\xi \approx 0.1$]. Parameters used are $t_0 = 3.1$ eV, $\alpha = 2.7$ eV/Å, $e_0 = 3.6$ eV, $\beta_M = 1.6$ eV/Å, $\beta_X = -0.8$ eV/Å, $K = 4.8$ eV/Å^2.

are interested in selecting a mass ratio which characterizes a real MX material, like PtBr. For our model calculations we used $\sigma_0 = m^*/m_X = 1.66$ and, consequently, $m^*/m_M = 0.34$, which is about the real mass ratio when X=Br and M=Pt. We choose the scaling force constant f^* [Eq. (A11)] to be equal to $2K$. Using $t_0 = 3.1$ eV, these values lead to $\xi \equiv 2t_0/(\hbar\omega^*) \approx 360$. Note that ξ is the only ω^*-dependent factor in the functional $\langle H \rangle$ after introducing dimensionless variational parameters $A_{ls}\alpha/(t_0 m^*\omega^*)$, $W_l\alpha/(t_0 m^*\omega^*)$, and $u_l\alpha/t_0$ [Eqs. (A1b) and (A9c)]. Since $\xi \propto \sqrt{m^*}$, varying this quantity is equivalent to varying the total mass of a MX unit (isotope effect at constant mass ratio), where we shall refer to ξ as an adiabaticity parameter: It is known from small polaron theory as the characteristic energy ratio. There a $\xi < 1$ is required. To study the connection between a *real* value of ω^* (i.e., $\xi = 360$) and the antiadiabatic limit of large ω^* (i.e., ξ small), we varied ξ between 0.1 and 360. We used the parameter set t_0=3.1 eV, α=2.7 eV/Å, e_0=3.6 eV, β_M=1.6 eV/Å, $\beta_X = -0.8$ eV/Å, K=4.8 eV/Å^2. In dimensionless notation (Table I), this is $e_0/(2t_0)$=0.6, $\beta_M/(2\alpha)$=0.3, $\beta_X/(2\alpha)$=−0.15, $Kt_0/(2\alpha^2)$=1. As in Sec. IV A 2 we found that for very small ξ and not too large U, the VAQP yields a lower bound for the ground-state energy than the EDCP. The antiadiabatic regime is described

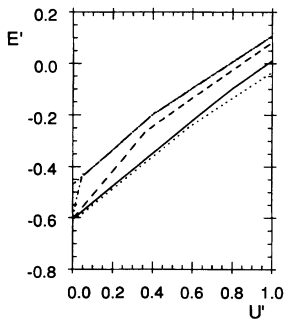

FIG. 12. The upper bound to the ground state energy as a function of Hubbard U, obtained by EDCP (solid) and VAQP for $\xi \approx 0.1$ (dotted), $\xi \approx 1$ (dashed), $\xi \approx 10$, (dash-dotted), $\xi \approx 360$, (dash-triple-dotted). Other parameters as in Fig. 11.

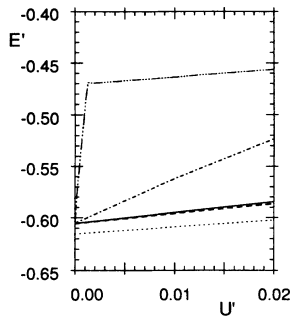

FIG. 13. An enlargement of the dip region of Fig. 12.

by $\xi \approx 0.1$, where VAQP is below EDCP almost up to $U \approx 7.2$. The relative quantum gain, defined as in Fig. 3(c), is shown for the antiadiabatic region in Fig. 11. Figure 12 demonstrates the behavior of VAQP away from the antiadiabatic region. The value of the VAQP energy bound approaches the value obtained by EDCP at U=0 for small phonon frequencies, as expected since, for U=0 and ξ=∞, the two approaches are the same. However, for finite U and larger phonon frequencies the VAQP lies above the EDCP. As U approaches 0 from above, the difference remains large until very close to $U = 0$, where the VAQP energy dips steeply to the EDCP value at U=0. The width of this dip decreases rapidly with increasing total mass. Figure 13 shows an enlargement of the dip region of Fig. 12.

In Fig. 14, we compare the expectation value of the VAQP lattice displacement amplitude, $\langle \Delta_l \rangle = \langle \Psi | (\hat{x}_{l+1} - \hat{x}_l) | \Psi \rangle$ [where $|\Psi\rangle$ is defined in Eq. (A5)] to the classical value found by EDCP as a function of U on eight-site systems for several ξ between 0.1 and 360. For all ξ, a pure CDW is found at U=0 by both methods. For finite U, $\langle \Delta \rangle$ is substantially reduced by quantum lattice phonons, and shows a steep drop to a predominantly AF phase at smaller U than Δ as found by EDCP does. Again the influence of quantum fluctuations contained in the VAQP removes the BOW phase, found by EDCP near $U = 0.88$. It is interesting to note that the EDCP-CDW amplitude (recall EDCP is an adiabatic treatment) drops to a phase of no distortion near $U = 1$, whereas

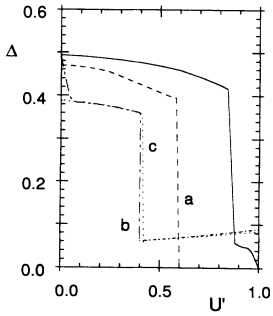

FIG. 14. Average QPVA lattice displacement amplitude, $\langle \Delta \rangle$, in comparison to the classical value found by EDCP (solid) on 8 sites with periodic-boundary conditions, for $e_0/2t_0$=0.6, $\beta_M/2\alpha$=0.3, $\beta_X = -\frac{1}{2}\beta_M$, $Kt_0/2\alpha^2$=1, and (a) ξ=0.1, (b) ξ=10, and (c) ξ=360.

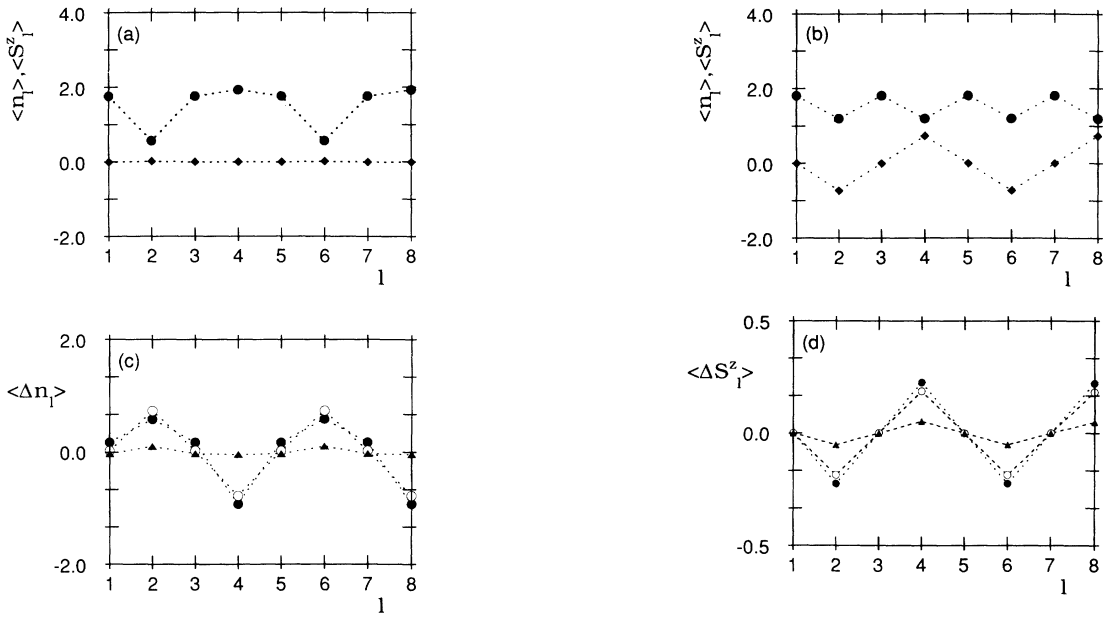

FIG. 15. (a) Total electronic VAQP density per site $\langle \Psi \mid n_l \mid \Psi \rangle \equiv \langle \Psi \mid n_{l\uparrow} + n_{l\downarrow} \mid \Psi \rangle$ (circles) and expectation value of the z-component of the spin operator at site l $\langle S_l^z \rangle$ (diamonds) for $\xi = 0.1$ and $U = 0.4$, (b) same as (a) but for $U = 0.6$, (c) difference $\langle \Psi \mid \Delta n_l \mid \Psi \rangle$ of $\langle \Psi \mid n_l \mid \Psi \rangle$ at $U = 0$ and at $U = 8.0$ (full circles) $U = 0.6$ (open circles) $U = 0.4$ (triangles) and $\xi = 0.1$, (d) difference $\langle \Delta S_l^z \rangle$ of $\langle S_l^z \rangle$ at $U = 0$ and at $U = 8.0$ (full circles) $U = 0.6$ (open circles) $U = 0.4$ (triangles) and $\xi = 0.1$.

in the adiabatic regime the VAQP approach finds a transition to a mixed CDW/SDW phase out to quite large U values, though the amplitude of the CDW becomes very small. As U approaches infinity, the VAQP appears to approach the $\frac{3}{4}$-filled SDW-Heisenberg limit, i.e., the X sites, with lower on-site energy, are doubly occupied whereas the M sites are singly occupied and show antiferromagnetic order. Within this mixed phase, we find a drop of the VAQP-CDW amplitude near $U = 0.4$ which is slightly ξ dependent (for $\xi > 1$). For $\xi > 1$ the $U = 0$ value of Δ equals that of the EDCP result; for $\xi < 1$ it is lower (i.e., reduced by quantum fluctuations). In the adiabatic region the VAQP-CDW lattice amplitude drops from its $U = 0$ value to a smaller one within an U interval which narrows as a function of ξ.

Figures 15 and 16 demonstrate both the total electronic VAQP density $\langle \Psi \mid n_l \equiv \langle \Psi \mid (n_{l\uparrow} + n_{l\downarrow}) \mid \Psi \rangle$ (circles) and the expectation value of the z component of the spin operator $\langle S_l^z \rangle = \langle \Psi \mid (n_{l\uparrow} - n_{l\downarrow}) \mid \Psi \rangle$ (diamonds) as a function of lattice sites for the same ξ values as in Fig. 14 and various values of U. The transition from pure CDW character at small U to mixed CDW/SDW ("spin-Peierls") character for larger U is evident. Figures 15(a) and 15(b) show the CDW behavior and the mixed CDW/SDW phase near the transition region for $\xi = 1$. Note that this transition is connected to the jump of the CDW amplitude near U=0.5 in Fig. 14 (symmetry change). Figures 15(c) and 15(d) show the deviation of $\langle \Psi \mid n_l$ and $\langle S_l^z \rangle$, respectively, from their U=0 behavior for several values of U. This deviation is largest for the largest U shown. Figure 16(a) demonstrates the effect of varying ξ on the total electronic VAQP density for $U = 1.0$. One finds that the adiabatic region begins as low as $\xi = 10$, since the densities are essentially independent of ξ for ξ values larger than this. The same effect on $\langle S_l^z \rangle$ can be seen in Fig. 16(b). This behavior is found to be similar for larger U values.

In the EDCP approach, no average magnetization is

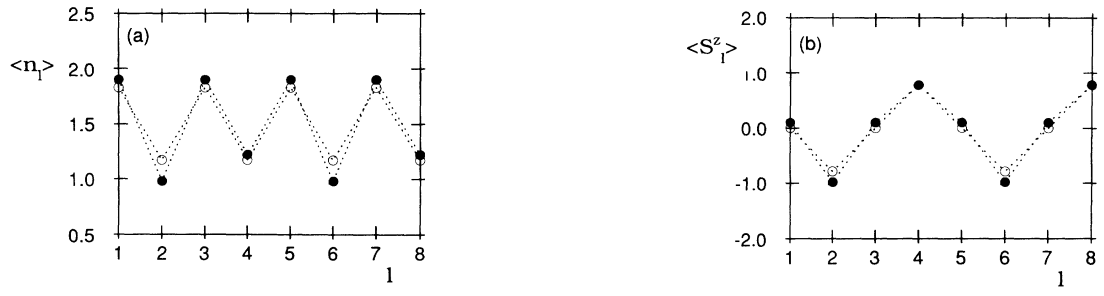

FIG. 16. (a) $\langle \Psi \mid n_l \mid \Psi \rangle$, and (b) $\langle S_l^z \rangle$, as a function of the lattice sites for $\xi = 360$ (full circles) and $\xi = 0.1$ (open circles).

found, but the spin-spin correlation functions are nonzero, even at U=0, with antiferromagnetic correlations between neighboring MM, MX, and XX sites. As a function of Δ, one finds a transition from the $\Delta = 0$ phase with dominant MM antiferromagnetic correlations to the large Δ phase where the XX antiferromagnetic interaction dominates, accompanied by a reduction of the average X occupancy. This agrees with the transition seen in the VAQP approach (and the HFCP approach), but leads to an interesting reinterpretation in terms of frustration.[32] Viewed in this fashion, it is reasonable that the competition between the effective NN and NNN spin interactions ("J_{MX}","J_{MM}","J_{XX}") is a second driving mechanism for long-period phases at commensurate filling, and in fact evidence of this mechanism driving such long-period phases has been found in our preliminary investigations.[32] The importance of competing spin interactions in the presence of lattice distortions (spin-Peierls phases), with the concomitant potential for inducing pairing as an alternate pathway to long-period phases, is also interesting in the context of the oxide superconductors; indeed, spin-Peierls mechanisms for driving the superconductivity have been previously discussed.[42]

2. *Other adiabatic methods*

The EDCP ground state was reviewed above in comparison to the VAQP; we do not reiterate those results here. Further, the HFCP, PTCP, and EDCP results for the ground state agree within the ranges where the HFCP and PTCP are valid (as can be seen, e.g., from the agreement in Fig. 3). For the ground state in HFCP we can define $U = 0$ effective parameters which yield the identical HFCP ground state as $U \neq 0$. Briefly, for CDW, BOW, or SDW distortions, we can, in general, write

$$\Delta(\ell) = d_X\left[\cos\left(\frac{\pi}{2}\ell\right) - \sin\left(\frac{\pi}{2}\ell\right)\right] + d_M\left[\cos\left(\frac{\pi}{2}\ell\right) + \sin\left(\frac{\pi}{2}\ell\right)\right] . \quad (12)$$

$$\rho(\ell) = (\rho_M + \rho_X)/2 + (-1)^\ell(\rho_M - \rho_X)/2 + \delta\rho_M\cos\left(\frac{\pi}{2}\ell\right) + \delta\rho_X\sin\left(\frac{\pi}{2}\ell\right) . \quad (13)$$

For the CDW, the lattice distortion amplitude is $\Delta = d_X$, $\delta\rho_X = 0$, and $(\rho_M + \rho_X) = 3$. If we insert these formulas into the Hamiltonian and assume ρ is spin independent (AF but not pure SDW phases are still allowed), we can rewrite the on-site terms as

$$[(-1)^\ell e_0 + \beta_\ell(\Delta_\ell + \Delta_{\ell-1}) + U_\ell\rho_{\ell\sigma}]n_{\ell\bar{\sigma}} \rightarrow \left[(-1)^\ell\left(e_0 + \frac{U_M\rho_M - U_X\rho_X}{4}\right) - \left(\beta_M - \frac{U_M\delta\rho_M}{4d_X}\right)2d_X\cos\left(\frac{\pi}{2}\ell\right) - \left(\beta_X - \frac{U_X\delta\rho_X}{4d_M}\right)2d_M\sin\left(\frac{\pi}{2}\ell\right)\right] n_{\ell,\bar{\sigma}} . \quad (14)$$

The HF correction to the total energy can be similarly rewritten, and we find $U = 0$ effective parameters as shown in Table I. Thus we can apply the $U = 0$ analysis of the phase diagram from paper I directly, noting that the effective parameters can have negative β, and so the possibility of a BOW phase for small K_{MM} is recovered. Numerical investigation using HFCP and EDCP shows that a transition to a BOW phase as U is increased can indeed occur before the lattice distortion vanishes. However, at least for some parameters, this is a small system size effect.

Within HFCP we have also looked at the predicted frequencies for the adiabatic phonon modes of the ground state, focusing on the $q = 0$ Raman (R) and infrared (ir) active modes (M-M and X-X in-phase and out-of-phase vibrations). In particular, the R active X-X out-of-phase stretch mode corresponds to oscillations of the CDW lattice distortion order parameter. While detailed studies of the trends and the comparison to experimental values is not complete, we note that for the PtCl parameters of Table II, the predicted frequencies are roughly 20% too small, though with finite U, such as the parameters scaled to $U_M = 0.5t_0$ in Table III, better agreement can be obtained. (The phonon frequencies are not invariant under the mapping of Table I.) For PtI, the $U = 0$ parameters give good agreement with the experimental frequencies.

V. DEFECT STATES: TRENDS IN THE MX MATERIALS

We now turn to considering the properties of intrinsic defects (polarons, bipolarons, and kinks) in the ground-state phases discussed above, caused by doping and/or, for kinks, topology. We describe the systematics of going from the strongly distorted charge-density-wave limit to the undistorted spin-density-wave limit in comparison to the experimental variation in the PtCl, PtBr, and PtI and the NiCl and NiBr series. (We are not aware of any reports of synthesis of NiI complexes.) A brief report of the systematics of increasing delocalization in comparison to the experimental variation in the PtX series may be found in Ref. 43, as well as a detailed report of the $U = 0$ systematics in paper I.

As noted above, the $U = 0$ effective parameters we define in Table I give the same band-structure and charge densities as $U \neq 0$ for the CDW ground state; the predicted absorptions for defect states, however, are different, and thus the $U = 0$ defect results in paper I cannot be simply interpreted as at an effective finite U. However, this does not imply that HFCP results do not capture the flavor of e-e correlations, but merely that local states are affected more strongly by e-e interactions than delocalized band states. As demonstrated in Fig. 17, the agreement between predicted absorption spectra in HFCP and EDCP out to intermediate values of the e-e correlations is excellent. The above ground-state analysis also indicates that QP corrections, as far as they are contained in our VAQP treatment, can be expected to be not extremely important for a description of the ground state properties of the MX materials. In fact, we find for the parameter region in which many of these materials are

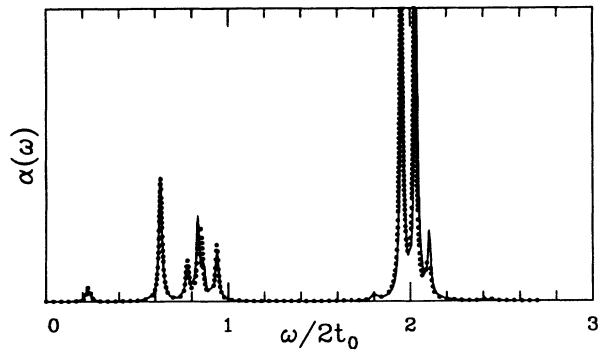

FIG. 17. Comparison of P^- absorptions calculated by EDCP (solid) and HFCP (dotted) on a 12-site ring for parameters with intermediate correlation strength: t_0=0.5, α=0.5, e_0=0.6, β_M=0.3, β_X=−0.15, K=1.0, K_{MM}=∞, and U_M=U_X=0.2. The three polaron peaks below the IVCT gap (at ∼ 0.8) are clearly visible, though the "bands" consist of only a few (Lorentzian broadened) lines.

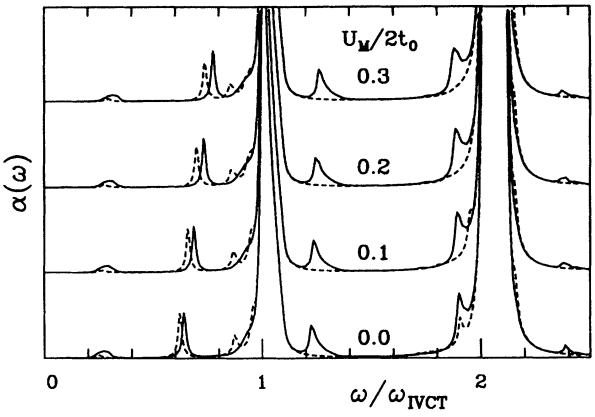

FIG. 18. U_M dependence of the optical absorption of electron (dashed) and hole (solid) polarons for e_0=0.6, β_M=0.3, K_{MM}=∞, and Δ=0.6 at U_M=U_X=0. The scaling in Table I was used to remove effects of increasing U_M on the band.

believed to lie, $U/t_0 \lesssim 1$ and $\xi \gg 0$, all methods (HFCP, EDCP, PTCP, and VAQP) agree. Thus, and since the EDCP method is limited to relatively small systems (at *most* 20 sites at $\frac{3}{4}$ filling), where finite-size effects tend to obscure the defect state properties, we focus here on results obtained within the HFCP method, calculated as described in Sec. II and Appendix C. We show below that the qualitative behavior predicted in HF approximation as the materials become more delocalized is not significantly altered at small to intermediate U from that at $U = 0$ discussed in paper I, as long as the lattice distortion amplitude is not too small. With the introduction of e-e correlations, we have however the additional possibility of the competing SDW phase and its attendant excitations, discussed in Sec. V C below, where EDCP treatment may prove essential.

The discussion here is more relevant for the PtI (intermediate e-ph) materials, whereas the PtCl (strong e-ph) materials were well described by the $U = 0$ analysis of paper I. We expect the Pd materials will also lie in the intermediate e-e/e-ph region where HFCP may still be reliably used, since experimentally they tend to exhibit a small degree of lattice distortion comparable to the PtI materials. Studies to determine parameters appropriate to the Pd materials are underway. While we discuss mean-field results for strongly e-e coupled systems below, for these (AF or SDW) materials such as NiBr, it will be important to properly treat e-e correlations to fully understand this region, and a systematic study is underway of just how well Hartree-Fock approximation captures the essence of strong e-e correlations in $\frac{3}{4}$-filled bands. We hope the mean-field results presented here will serve as a guide to both understanding the real materials and interpreting and focusing the more calculationally intensive EDCP studies of the predicted defect properties. Preliminary results indicate[32,44] that strong further neighbor terms can lead to ground-state phases, and that introduction of defects near ground-state phase boundaries can push the system across the boundary. The properties of defects in the *anti*adiabatic limit are also under investigation with VAQP.

A. Trends in Hartree-Fock: Effects of increasing U within the CDW phase

In Fig. 18, we show the variation in the predicted optical absorption for electron and hole polarons ($P^{\pm}$) as the Hubbard U is increased to intermediate e-e coupling strength for a parameter set relevant at $U = 0$ to a strongly electron-phonon coupled MX material. The spectra were normalized to the M-band to M-band transition edge (IVCT band edge, ω_{IVCT}, or optical gap, E_g). The effects of U on the uniform properties were removed by using the scaling defined in Table I for effective $U = 0$ parameters to keep the uniform band structure, optical gap, lattice distortion, and charge density fixed. For comparison, we show in Fig. 19 the energy-level diagram. The

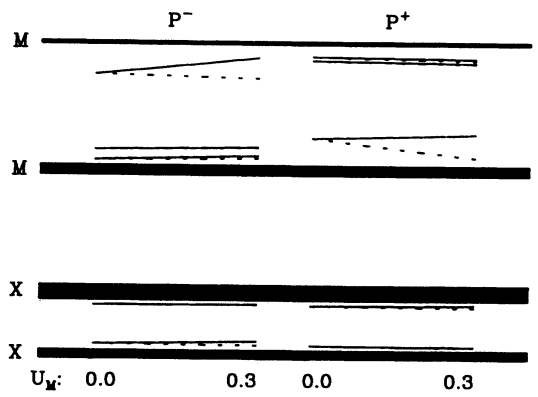

FIG. 19. Effect of the Hubbard U_M on the energy-level diagram for polaronic defects using the same parameters as Fig. 18. Up- (dashed) and down- (solid) spin states split for $U_M > 0$, where the unpaired electron is defined to have spin up.

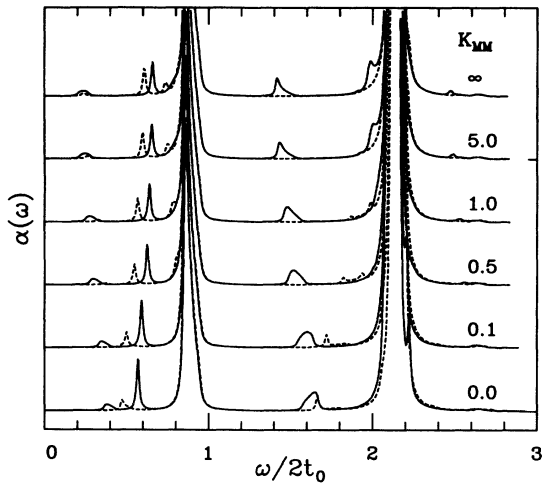

FIG. 20. K_{MM} dependence of the $P^{\pm}$ optical absorption for the parameters of Fig. 17 with U_M=0.2 and U_X=0.0.

energies of the localized levels for spin up and down split nearly linearly in U. The M-band to M-band transition (IVCT band) is only $0.1\omega_{\mathrm{IVCT}}$ wide. (Note for PtCl,[45] the band width is $\lesssim$0.5 eV while the gap is ~2.5 eV.) The peak around $2\omega_{\mathrm{IVCT}}$ is due to the upper X-band to M-band transition. The transition from the lower X-band to the conduction M band (at $2.4\omega_{\mathrm{IVCT}}$–$2.6\omega_{\mathrm{IVCT}}$) is very weak, and does not show on this scale. The structure of the band-to-band transitions is cut off in this figure, but both show square-root singularities due to the density of states at the band edges, which is lost at the higher end of the IVCT (M-M) absorption due to both a vanishing matrix element and an increasing frequency (see, e.g., Fig. 3). Thus the IVCT has the "triangular" shape familiar from $\frac{1}{2}$-filled bands, and the nonzero X-M absorption band has a more textbook 1D band "U" shape. The intragap features below ω_{IVCT} and the ultragap features between the IVCT and X-M absorption bands, as well as above the allowed X-M absorption band, are due to transitions to and from the local polaronic states introduced in the M-M and X-X gaps (see Fig. 19). There are no local states split off (at least, not significantly) from the outer band edges or into the M-X gap. Increasing e-e correlations shift the "A" peak[45] (local-local intragap transition) structure to higher energies and increase the e/h asymmetry. If we had just added a Hubbard U without the scaling of Table I, the gap edge would move to lower frequencies while the A peak energy would remain relatively unchanged. This agrees with the trends expected from a $t_0 = 0$ analysis[7,44] since there the polaronic local-local state transition yields no change in the contribution of U to the total energy. The local change in charge density and lattice distortion due to the polaron show corresponding small shifts from the $U = 0$ value.

For this same parameter set, we show in Fig. 20 the variation in the predicted $P^{\pm}$ optical absorptions for a representative Hubbard U as the NNN spring K_{MM} (due to the ligand-ligand steric repulsion) is varied, and in Fig. 21 we compare for the two limiting values of K_{MM} the $P^{\pm}$ intragap absorptions with the predicted intragap optical absorption of electron and hole bipolarons ($B^{\pm}$) and electron, hole, and neutral solitons or kinks ($K^{\pm,0}$). For simplicity, we did not use the effective $U = 0$ parameter scaling, and the gap in Fig. 20 shows the decrease due to U. Recall that the value of K_{MM} has no effect on the CDW ground-state phase. However, the defect absorptions at $K_{MM} = 0$ and $K_{MM} = \infty$ are very different, though for $K_{MM} \gtrsim K$ from Fig. 20 we see they are insensitive to the exact value of K_{MM}. As $K_{MM} \to 0$ defect absorptions move to the gap center or edge, as also observed at $U = 0$ in paper I. We feel, based both on the expectation that the ligand-ligand repulsion will be large and the agreement between predicted and measured optical-absorption spectra,[12] that $K_{MM} \to \infty$ is the best

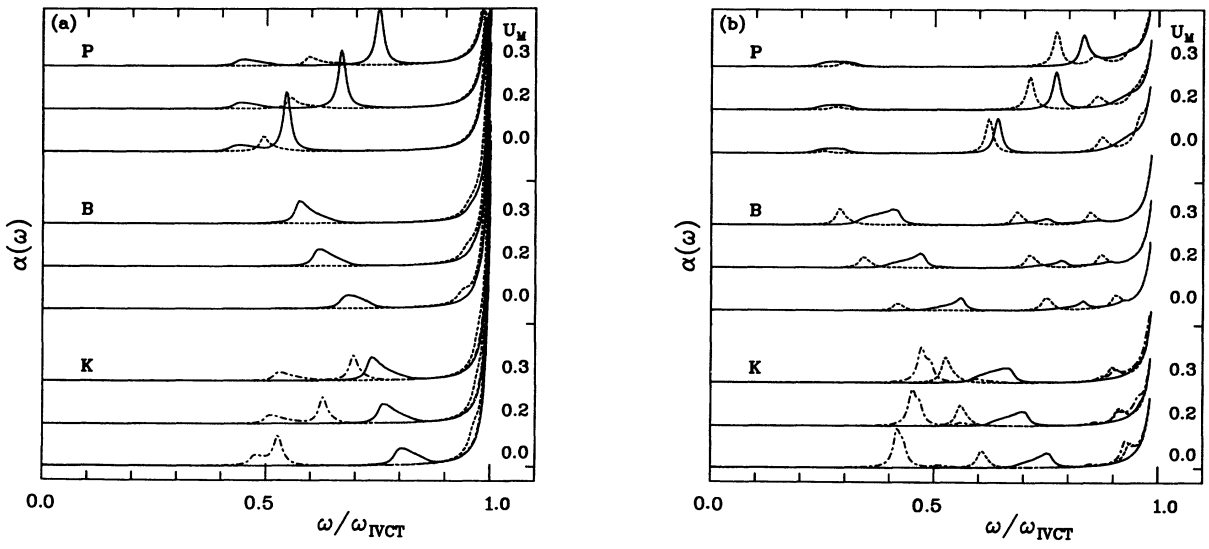

FIG. 21. U dependence of the P, B, and K optical absorption for the parameters of Fig. 17 with (a) K_{MM}=0 and (b) K_{MM}=∞. Hole defect curves are solid, electron defects dashed, and neutral defects are dashed-dotted.

value of K_{MM} to use for modeling MX chains, at least until the analysis of phonon modes, which are more sensitive to the exact value of K_{MM}, has been completed.

The systematics seen in HFCP going from strongly e-ph distorted materials to strongly e-e coupled materials, focusing on parameters relevant to particular MX materials, is discussed in the next two sections, again with the caveat that the results for *large* U will not be quantitatively, but should be qualitatively, correct.[44]

B. Defects in electron-phonon dominated regime: The PtX materials

Figure 22 shows the predicted optical absorptions for the trend PtCl, PtBr, and PtI using the effective $U = 0$ HF parameters of Table II, but scaled to $U_M = t_0/2$ as in Table III, since we expect this to be roughly true for the Pt materials. The absorptions for $U_X = U_M$ (with the parameter scaling to give the same uniform properties) are not significantly different from $U_X = 0$. The general trends from the $U = 0$ predicted absorptions discussed in paper I remain. In the strongly distorted case, the M-X transition is strong and polarons tend to have three intragap peaks, with the A peak being the strongest intragap absorption. This changes smoothly as the weakly distorted case is approached. The M-X transition decreases in oscillator strength and is essentially lost for very weak electron-phonon coupling. For polarons, the high-energy intragap (B) peak shifts upwards and merges into the band for very weak e-ph coupling, and the low-energy intragap (C) peak gains in intensity till it has oscillator strength roughly equal to the A peak. However, the asymmetry between electron and hole defect absorptions is enhanced over that seen at $U = 0$, and the defect absorptions are shifted slightly by U, as discussed above for the strongly distorted case. In Fig. 23 we show the absolute absorptions of the PtX materials (oscillator strength per M_2X_2 unit) with polarons, where we have added the lines from the P^+ and P^- and broadened to produce "experimental" spectra. The trend to decreasing height and narrowing of the IVCT as the gap gets larger agrees well with experiment.[46]

Figure 24 shows the the CDW lattice distortion order parameters (i.e., the amplitudes of the CDW components of the lattice distortion) corresponding to the polaron absorptions just discussed. The hole defects are somewhat broader, though this effect is more noticeable on the charge distribution since, for holes, it is difficult to remove charge from the nearby halides as they are lower in energy and the defect is forced to spread out to further neighbor metals, whereas, for electron defects, excess charge flows more easily onto the halides (though strong U_X will of course change this argument). Thus this is understandable as a two-band effect, which should be most noticeable for intermediate localization. The charge and spin distributions for the PtBr parameters are shown in Fig. 25, where this effect is easily seen. For the PtI parameters, the defects are broad and insensitive to the position of the center. For example, the two phases of the P^- polaron defect shown in Fig. 26 have

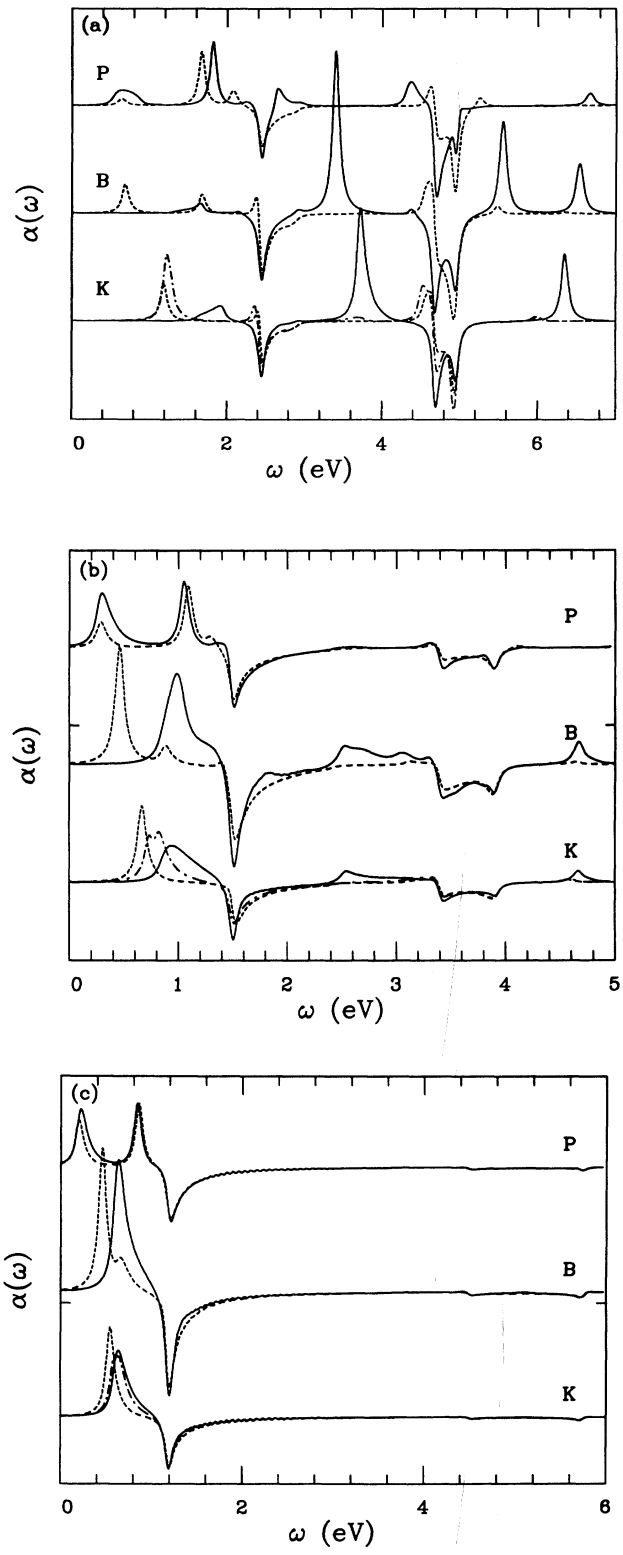

FIG. 22. Predicted absorption of P, B, and K defects for the CDW materials (a) PtCl, (b) PtBr, and (c) PtI using the parameters of Table III at $U_M = t_0/2$. Difference spectra with the uniform absorption subtracted off are shown to enhance the structure due to defect absorptions. Hole defect curves are solid, electron defects dashed, and neutral defects are dashed-dotted.

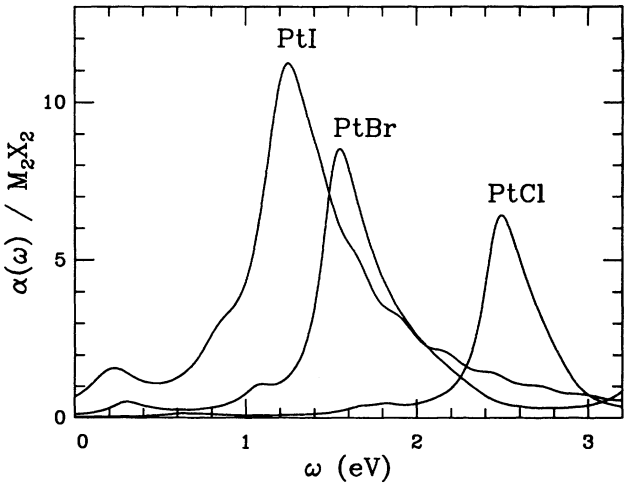

FIG. 23. Absolute absorptions per unit cell (M_2X_2 unit) for the PtX materials using the parameters of Table III. Here we have added the $P^{\pm}$ lines and broadened to produce "experimental" spectra. The trend to decreasing height and narrowing of the IVCT as the gap gets larger agrees with experiment (Ref. 46).

the same energies and optical spectra, to numerical accuracy. The more strongly distorted, more valence localized materials—as seen from Fig. 24 defects for the PtCl parameters are localized over ~3 lattice sites—are sensitive to defect location with, e.g., the P^+ defects trapped on sites which would be reduced (occupied) if the chain were uniform. The B and K distortion show similar behavior, as discussed in paper I for $U = 0$.

C. Defects in electron-electron dominated regime: The NiX materials

Turning to the NiX complexes, in Fig. 27 we show the absorption predicted within HFCP for the uniform states and in Fig. 28 we show the predicted difference absorptions of the SDW $P^{\pm}$ and $K^{\pm,0}$ defects for the trend NiCl and NiBr using parameters from Table III.

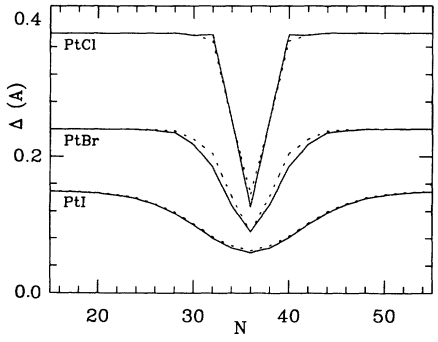

FIG. 24. Predicted P^+ (solid) and P^- (dashed) lattice distortions for the CDW materials PtCl, PtBr, and PtI using the parameters of Table III at $U_M = t_0/2$. The phase of the CDW lattice distortion order parameter for the P^+ defects was fixed to be 180° out of phase from the CDW on the P^- defects so that they fall on the same site to facilitate comparison of widths.

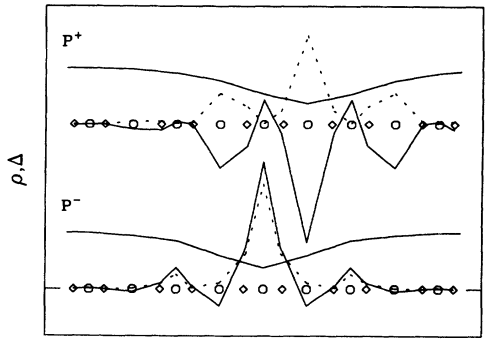

FIG. 25. Excess charge (solid) and spin (dashed) distributions (uniform chain values subtracted) of the P^+ and P^- defects for the intermediate CDW material PtBr (parameters of Table III). M (circle) and X (diamond) positions are indicated. The CDW lattice distortion order parameter from Fig. 24 is also shown for easier comparison. Note the hole defect is broader.

The $B^{\pm}$ were unstable and did not form for these parameters. Note that as there is no lattice distortion, the topological kinks ($K^{\pm,0}$) are between the two degenerate mean-field SDW phases ($XMXM\cdots = \uparrow\downarrow\ \uparrow\ \uparrow\downarrow\ \downarrow\ \cdots$ and $\uparrow\downarrow\ \downarrow\ \uparrow\downarrow\ \uparrow\ \cdots$). In Fig. 29, we show the corresponding energy levels for the NiBr parameters. Note that for polarons, down (solid) and up (dashed) spin states split off from the top of the conduction band and bottom of the lower Br band, respectively, where the unpaired electron is defined to have spin up, in contrast to the lack of such "ultragap" localized states for materials with non-zero lattice distortion such as the PtX materials discussed above. Ultragap states are also seen in Fig. 28 for the kinks, where here the K^0 shows the different shifts for the different spins, and the $K^{\pm}$ show the same shift for up and down spin as the levels are symmetrically occupied. As seen from Fig. 28, these ultragap states also have absorptions within the IVCT gap, complicating the spectra. The P^+ and K^+ show similar spectra, as do the

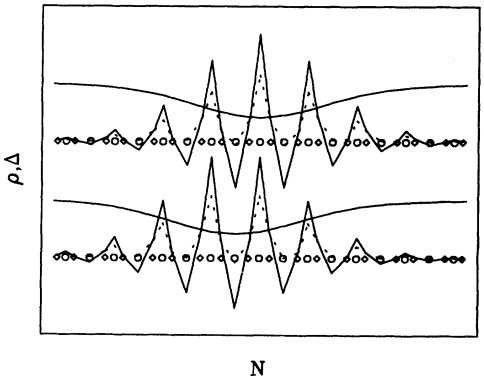

FIG. 26. The two phases of the P^- lattice distortions for the weakly CDW material PtI (parameters of Table III) shown here are equivalent to numerical accuracy. Excess charge (solid) and spin (dashed) distributions (the uniform chain values have been subtracted) are shown along with the lattice distortion amplitude. M (circle) and X (diamond) positions are also indicated.

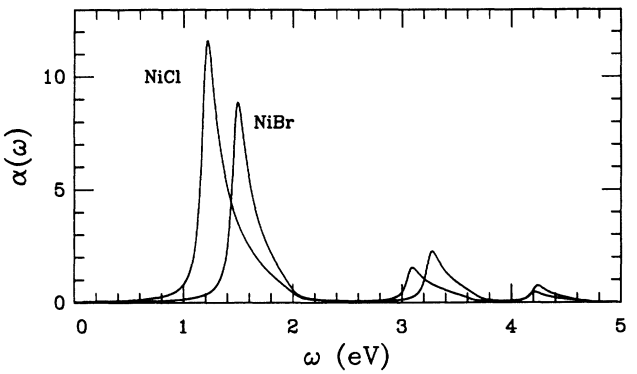

FIG. 27. Absolute absorptions per unit cell (M_2X_2 unit) for the uniform NiX materials using the parameters of Table III. Note in contrast to the CDW PtX materials, both M-X transitions are clearly observed, though unfortunately the gap size relation is the reverse of what is reported experimentally.

P^- and the K^- plus K^0. It appears that there is also structure within the bands, though this may be coming from the ultragap states having absorptions at similar energies.

The excess charge and spin distributions of the various defects are shown in Fig. 30. The SDW of the uniform lattice has been subtracted to better illustrate the perturbation caused by the defect. For the kinks at the defect center we have changed the phase of the subtracted SDW by 180°, so the structure may be interpreted as due to a fully relaxed kink in comparison to a sharp defect. The resultant pictures for the kinks and polarons look very similar, in agreement with the similarity observed in the absorption spectra. From Fig. 30 we also see that the amplitude of the local lattice distortion is very weak in comparison to the deviation in spin and charge. This is in contrast to the CDW materials where they are comparable. Even so, R and ir activity should be experimentally observable in the NiX materials. Both the NiBr and NiCl parameters of Table III yield similarly localized defects, though the e-ph interaction strength does vary by $\sim 20\%$. At the very least, they are an indication of how predicted properties of SDW defects should vary as the e-ph coupling is varied within the HFCP scheme at fixed ratio of $U/t_0 \sim 3$. A systematic study of the defects properties as α and β are varied for defects in the SDW phase has not been completed (obviously their value does not affect the uniform SDW phase), so we cannot draw any general conclusions at this time as to how the predicted distortions, and the corresponding absorptions, vary with increasing delocalization.

As stressed above, the strong e-e coupling HFCP results need to be tested against EDCP or other calculational techniques which treat e-e correlations better. These studies have begun,[32,44] though we still are at the stage of separating finite-size effects from true bulk behavior. Among the interesting questions under investigation in EDCP are whether the $K^{\pm}$ remain topologically distinct from the $P^{\pm}$ (and whether the K^0 can be defined), whether there is a region at strong coupling where bipolarons form, and the influence of U_M, U_X, V, α, and β on the answer to these questions—which are 1D versions of very similar questions being asked in the quasi-2D oxide superconductors. As noted in the section on parameters, the predicted optical gaps (NiCl: 1.2 eV; NiBr: 1.5 eV) do not agree with listed experimental values[29] as to their ordering, though the absolute values are, encouragingly, well within a factor of 2. However, preliminary EDCP results indicate that these gaps are also roughly a factor of 2 larger than the EDCP prediction, making the agreement less good. A slight CDW, or a larger difference in t_0 or e_0 could easily bring the disagreement back in line with the experimentally reported values, though further experiments are also necessary to confirm these gap as-

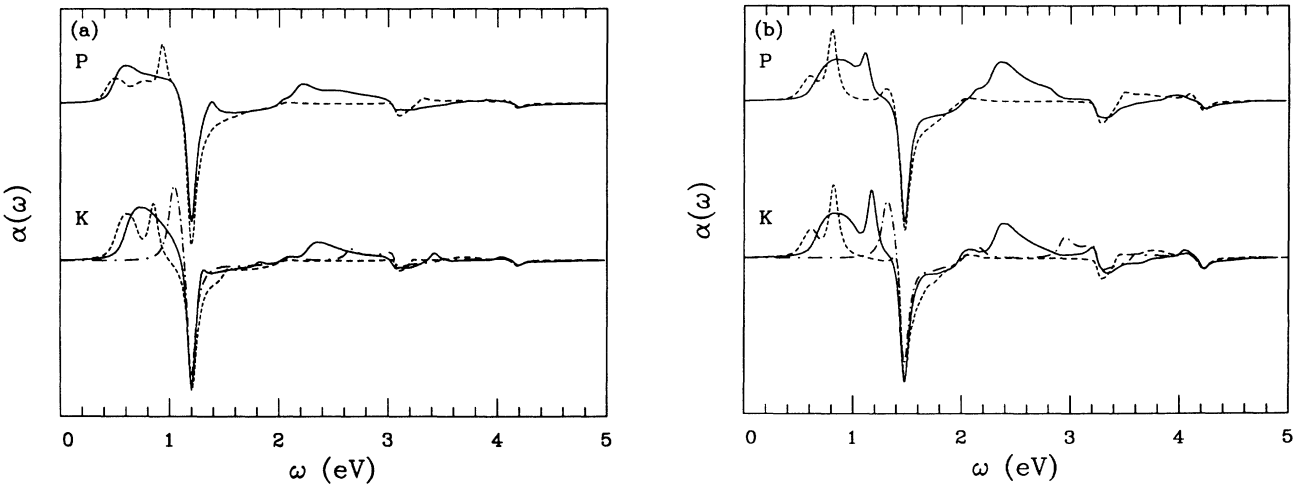

FIG. 28. Predicted absorption of $P^{\pm}$ and $K^{\pm,0}$ defects for the SDW materials (a) NiCl, (b) NiBr using the parameters of Table III. The $B^{\pm}$ defects do not form for these parameters. Difference spectra with the uniform absorption subtracted off are shown to enhance the structure due to defect absorptions. Hole defect curves are solid, electron defects dashed, and neutral defects are dashed-dotted.

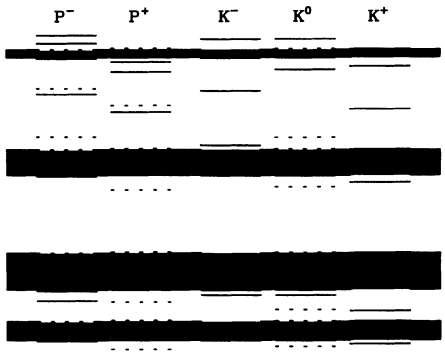

FIG. 29. Energy-level diagram for P and K defects using the NiBr parameters of Table III. Note down (solid) and up (dashed) spin states split off from the top of the conduction band and bottom of the lower Br band, respectively, where the unpaired electron is defined to have spin up.

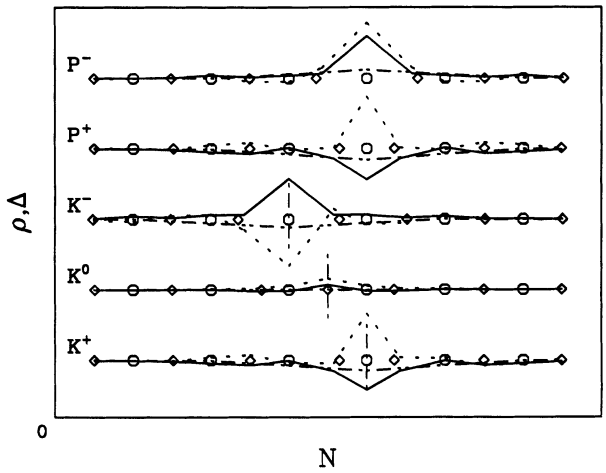

FIG. 30. HFCP predictions for the P and K lattice distortions (dash-dotted), excess charge (solid) and spin (dashed) distributions (uniform chain values subtracted) for the strongly e-e coupled (AF or SDW) material NiCl (parameters of Table III). M (circle) and X (diamond) positions are also indicated. The vertical bars denote where the phase of the uniform chain subtracted from the kink defects was shifted by 180° so as to give zero excess charge and spin far from the defect.

signments. It is intriguing to note that, within HFCP, for slightly stronger values of the electron-phonon coupling we found that a strong CDW was predicted for our NiX parameters. For the PtI parameters, we found a metastable SDW phase. Thus, these materials may well be near a phase boundary where interesting long-period and/or pairing behavior are more likely to be observed. We are currently examining the experimental data to see if there are signatures of the presence of competing phases in the real materials. Preliminary data on a PtI material indicates that there may indeed be unusual magnetic behavior: Haruki and Wachter[47] have reported 70% of perfect diamagnetism in one sample.

VI. CONCLUSIONS

The competing effects of strong electron-electron and electron-lattice interactions are of paramount concern in many electronic materials currently under investigation. This is particularly so in reduced-dimensional materials where there is a delicate competition for broken symmetry ground states. Learning to control material properties so as to tune into such ground states selectively, and to control the properties of self-trapped defects such as polarons and bipolarons (introduced by doping, photoexcitation, electrochemical doping, etc.) is essential to both synthesis and device applications.

In this paper we have begun to consider an explicit $\frac{3}{4}$-*filled, two-band*, extended Peierls-Hubbard Hamiltonian, which we believe is an important reference model for many electronic materials, including MX chain compounds, charge-transfer salts, and organic and oxide superconductors. We are discovering that the model is intrinsically richer than the frequently studied $\frac{1}{2}$-filled one-band models, exhibiting a variety of different broken-symmetry ground states, including charge-density-, spin-density-, and bond-order-waves, superlattice ordering (even at exactly $\frac{3}{4}$ filling), and complex spin-Peierls phases, in which lattice distortion and charge- and spin-density waves are all combined. In addition, there are intrinsic electron-hole asymmetries associated with doping around $\frac{3}{4}$ filling. All of these indications point to the need for a systematic understanding of commensurate multiband reference phases (for which the present model is a prototype), and the need for a close examination of the regimes of validity of reductions to effective one-band models.

Interestingly, the two-band situation does not exhibit many of the nonperturbative pathologies of the $\frac{1}{2}$-filled one-band case when Hubbard-type interactions are introduced. This means that when such interactions have modest strength, mean-field (e.g., HF) treatments are valid. Thus, many of the MX materials in the charge-disproportionated (CDW) phase can be well described by a HF approach, as we have confirmed by calibration against finite chain EDCP results. We are presently extending this modeling to include MX chain materials with stronger e-e interactions, where dominant *spin*-ordering (spin-density-wave or spin-Peierls) is observed (e.g., in NiCl or NiBr), and studies of correlation effects on the static (optical-absorption, ir, and Raman signatures) and dynamic (photodecay channels, conductivity) properties of nonlinear excitations (polarons, bipolarons, excitons, solitons) induced by doping and photoexcitation are underway. In this spin-interaction-dominated regime, mean-field treatments break down quantitatively (although not necessarily qualitatively even at relatively large interaction strengths) and extensive EDCP or quantum Monte Carlo analysis is necessary, although these techniques are limited numerically to small system sizes. For EDCP, exploiting symmetries of the Hamiltonian allows one to treat (slightly) larger system sizes, but we expect the most progress here to come from improved extrapolation.[48]

A further consideration is the validity of adiabatic

("frozen phonon") approaches to the two-band model. In this manuscript we have investigated nonadiabatic corrections within a variational approach (VAQP). Not surprisingly, in view of the large masses involved in MX chain materials, such corrections are negligible. However, more generally for small masses and strong correlations, systematic improvements on the VAQP are desirable. As shown in Sec. IV A, some analytic results are possible in the fully antiadiabatic regime, where unusual effective nonlinear lattice dynamics can result after integrating out electronic degrees of freedom. Comparison of results obtained by different theoretical approaches in two-band models including both electron-phonon and electron-electron interactions is a very urgent task, to enable further improvement of these methods.

Although we have focused our discussion on the broad *class* of MX chain compounds now available, it will be very important to apply some of the understanding we have gained to related low-dimensional materials. Organic superconductors display many of the same broken-symmetry ground states as a function of material properties (pressure, temperature, etc). Again, it is increasingly appreciated that electron-phonon interactions are very important in high-temperature superconducting compounds, both for the determination of ground states and the nature of the excitations. Just as in the present model, polaronic excitations created with respect to a CDW (SDW) ground state result in *local* relaxation into the SDW (CDW) phase also. This local phase-mixing is expected to be particularly interesting for the intermediate spin-Peierls phases, especially as regards the possible pairing of carriers.

In summary, the work presented here and in paper I is intended to help lay the theoretical ground work for our "making-measuring-modeling" effort toward understanding the MX chain class, which span the range from electron-phonon to electron-electron dominated materials. We also feel that the lessons and techniques reported here will lead to a more general microscopic understanding of nonlinear excitations in low-dimensional materials with strong competitions for broken-symmetry ground states, particularly the rich phases found in a $\frac{3}{4}$-filled two-band, versus a $\frac{1}{2}$-filled one-band, scenario.

ACKNOWLEDGMENTS

We would like to thank the many people who have collaborated in this research effort, including R.C. Albers, M. Alouani, M. Aronson, I. Batistić, C. Boyle, S. Conradson, R.J. Donohoe, P.J. Hay, S.C. Huckett, S. Marianer, R.J. Martin, S.R. Phillpot, J. Reichl, H. Röder, A. Saxena, B.I. Swanson, D. Tait, and L. Worl; as well as thank, among others, D. Baeriswyl, H. Büttner, D.K. Campbell, M. Haruki, K. Iwano, M. Kurita, T. Mitani, K. Nasu, X. Sun, A. Terai, and Y. Wada for useful discussions. This work was supported by the U.S. DOE—Office of Basic Energy Sciences, and by the Deutsche Forschungsgemeinschaft through SFB 213 (TOPOMAC, Bayreuth). We are also happy to acknowledge the Centers for Materials Science and Nonlinear Studies for computational support at Los Alamos National Laboratory, the Höchstleistungsrechenzentrum (HLRZ) at the KFA Jülich, Federal Republic of Germany and the Leibniz-Rechenzentrum München (LRZ), Federal Republic of Germany for computational support. Travel funds for J.T.G. for collaborative research were provided in part by the Estate of Elsie G. Hall. S.M.W.-M. wishes to acknowledge the hospitality of the Center for Nonlinear Studies and the Theoretical Division at Los Alamos National Laboratory, where parts of the present work were done. J.T.G. and A.R.B. acknowledge the hospitality of the Physics Department of the University of Tokyo and the Institute for Molecular Science in Okazaki, where extensive discussions on this subject of mutual interest, MX chains, were held.

APPENDIX A: VARIATIONAL METHOD

In this appendix we briefly describe the formulation of our quantum phonon variational *Ansatz* (VAQP). The VAQP has the advantage that it is applicable to large systems, since the resulting energy functional has the form of a one-particle Hamiltonian for the electrons — the phonon degrees of freedom are mapped onto variational parameters. For simplicity, for the discussion in this paper we set $V = 0$ and concentrate on contrasting the effects of quantum phonon fluctuations with the effects of electron-electron correlations described by the Hubbard U. The VAQP including a Hubbard V can be formulated similarly, and is currently under investigation.

The first step in the construction is to perform a change of basis in the underlying Hilbert space by applying a suitable unitary transformation to remove exactly all explicit electron-electron correlation terms. We define a class of unitary transformations (see Refs. 23 and 49) by

$$\hat{O} \equiv \prod_{l,s} \hat{O}_{ls}\{A_{ls}\}, \tag{A1a}$$

where

$$\hat{O}_{ls}\{A_{ls}\} \equiv \exp\left(\frac{i}{\hbar} A_{ls} \hat{x}_l \, n_{ls}\right) \tag{A1b}$$

with real variational parameters A_{ls}. This transformation has the following effects on the momentum, displacement and Fermi operators:

$$\hat{O}\hat{P}_l\hat{O}^\dagger = \hat{P}_l - \sum_s A_{ls} n_{ls} \ , \tag{A2a}$$

$$\hat{O}\hat{x}_l\hat{O}^\dagger = \hat{x}_l \ , \tag{A2b}$$

$$\hat{O}c^\dagger_{ls}\hat{O}^\dagger = \exp\left(\frac{i}{\hbar} A_{ls}\hat{x}_l\right) c^\dagger_{ls} \ . \tag{A2c}$$

The electronic density n_{ls} is invariant. Applying the unitary transformation $\hat{O}$ to the Hamiltonian H [Eq. (1) with $V = 0$], if we chose

$$A_{l\uparrow}A_{l\downarrow} = -M_l U_l \ , \tag{A3}$$

then in the transformed Hamiltonian, $\tilde{H} \equiv \hat{O}H\hat{O}^\dagger$, all explicit correlation terms are removed:

$$\tilde{H} = \sum_{l,s}\{[-t_0 + \alpha(\hat{x}_{l+1} - \hat{x}_l)]e^{i\hat{\phi}_{ls}}\, c^{\dagger}_{l+1s}c_{ls} + \text{H.c.}\} + \sum_l [\varepsilon_l - \beta_l(\hat{x}_{l+1} - \hat{x}_{l-1})]\, n_l$$
$$+ \sum_{l,s}\left(\frac{1}{2M_l}(A_{ls} - 2\hat{P}_l)A_{ls}\right) n_{ls} + \sum_l \left(\frac{\hat{P}_l^2}{2M_l} + \frac{K}{2}(\hat{x}_{l+1} - \hat{x}_l)^2\right) + \frac{1}{2}K_{MM}\sum_l (\hat{x}_{2l+2} - \hat{x}_{2l})^2 \,, \tag{A4}$$

where $\hat{\phi}_{ls} \equiv (1/\hbar)(A_{l+1s}\hat{x}_{l+1} - A_{ls}\hat{x}_l)$.

The next step is to make a variational *Ansatz* for the form of the ground state wave function $|\tilde{\Psi}\rangle$ in this transformed basis. We choose $|\tilde{\Psi}\rangle$ to be a simple pure tensor product of phonon (boson) and electron (fermion) parts: $|\tilde{\Psi}\rangle = |B\rangle \otimes |F\rangle$. This choice ensures numerical efficiency of the *Ansatz* for larger system sizes: it allows us to construct a simple electronic effective one-particle Hamiltonian as the functional to be varied. The form of the variational wave function in the original basis now reads

$$|\Psi\rangle = \hat{O}^{\dagger}|\tilde{\Psi}\rangle = \hat{O}^{\dagger}\,|B\rangle \otimes |F\rangle. \tag{A5}$$

Here, $|B\rangle$ denotes a Bose state to be specified below and $|F\rangle$ denotes the electronic eigenfunction determined uniquely by the form of the functional $\langle H\rangle$ to be varied

$$\langle H\rangle = \frac{\langle\Psi|H|\Psi\rangle}{\langle\Psi|\Psi\rangle} \,. \tag{A6}$$

To make the *Ansatz* more transparent, we expand the exponential, obtaining

$$|\Psi\rangle = \prod_l [\,(e^{a_{l\uparrow}+a_{l\downarrow}} - e^{a_{l\downarrow}} - e^{a_{l\uparrow}} + 1)\otimes n_{l\uparrow}n_{l\downarrow}$$
$$+(e^{a_{l\uparrow}} - 1)\otimes n_{l\uparrow} + (e^{a_{l\uparrow}} - 1)\otimes n_{l\downarrow}$$
$$+1\otimes 1]\;|B\rangle\otimes|F\rangle \tag{A7}$$

with $a_{ls} \equiv -\frac{i}{\hbar}A_{ls}\hat{x}_l$. Comparing this to a Gutzwiller *Ansatz* for a purely electronic Hamiltonian,[50]

$$|F_G\rangle = \prod_l [1 - (1-g)\,n_{l\uparrow}n_{l\downarrow}]\,|\Psi_0\rangle, \tag{A8}$$

where $|\Psi_0\rangle$ denotes the ground state of the uncorrelated system, the extension of this *Ansatz* to quantum phonons is immediate. For $g = 1$ the Gutzwiller *Ansatz* projects out double occupancies from $|\Psi_0\rangle$, whereas the *Ansatz* (A5) and (A7) affects both the singly and the doubly occupied sites in $|B\rangle\otimes|F\rangle$, depending on the value of the parameters A_{ls}. It is important to stress that our variational wave function does not contain a Gutzwiller limit, since both the singly and the doubly occupied sites are affected. (A detailed comparison between the class of variational wave functions we use and Gutzwiller type approaches is under investigation.[51]) Note that a Gutzwiller *Ansatz* in combination with an adiabatic treatment of classical phonons was used in Ref. 52 to study the influence of electronic correlations in polyacetylene.

The properties of the variational *Ansatz* strongly depend on the form of $|B\rangle$. Here, we select

$$|B\rangle \equiv \prod_l |b_l\rangle, \tag{A9a}$$

where

$$|b_l\rangle \equiv |b_l(W_l, u_l)\rangle = \hat{U}_l\{W_l, u_l\}\,|0\rangle \,, \tag{A9b}$$

with the unitary transformation

$$\hat{U}_l\{W_l, u_l\} \equiv \exp\left(-\frac{i}{\hbar}(W_l\hat{x}_l - u_l\hat{P}_l)\right) \,. \tag{A9c}$$

Again, W_l and u_l are real variational parameters and $|0\rangle$ denotes the multiphonon vacuum state. This choice is one of the simplest; more general ones have been tested for small system sizes.[51,53] More "complicated" choices for $|B\rangle$ improve the quality of the energy bound only in limited regions of the model parameter space; there also exist parameter ranges where the results of the present simple form cannot be improved. Nevertheless, more general choices are being tested for the two-band model under investigation.

Finally, the expectation value of the total energy is minimized with respect to the variational parameters. The functional $\langle H\rangle$ to be minimized contains $3N$ free variational parameters ($\{A_{l\uparrow}, W_l, u_l\}$) which have to be determined. The partial expectation value $\langle B|\,\tilde{H}\,|B\rangle$ now reads

$$\langle B|\,\tilde{H}\,|B\rangle = \sum_l [\varepsilon_l - \beta_l(u_{l+1} - u_{l-1})]\,n_l + \sum_{l,s}\left(\frac{1}{2M_l}(A_{ls} - 2W_l)A_{ls}\right) n_{ls}$$
$$+ \sum_{l,s}\left[\left(-t_0 + \alpha(u_{l+1} - u_l) - \frac{i\alpha}{2m^*\omega^*}(A_{l+1s} + A_{ls})\right)e^{-\Phi^2_{ls}}\, c^{\dagger}_{l+1s}c_{ls} + \text{H.c.}\right]$$
$$+ \sum_l \left(\frac{1}{2M_l}W_l^2 + \frac{K}{2}(u_{l+1} - u_l)^2\right) + \frac{1}{2}K_{MM}\sum_l (u_{2l+2} - u_{2l})^2 + E_0 \,, \tag{A10}$$

where

$$\omega^{*2} \equiv \frac{f^*}{m^*} , \tag{A11}$$

$$m^* \equiv \left[\frac{1}{2}\left(\frac{1}{M_M} + \frac{1}{M_X}\right)\right]^{-1} , \tag{A12}$$

$$\Phi_{ls}^2 \equiv \frac{A_{l+1s}^2 + A_{ls}^2}{4m^*\omega^*\hbar} . \tag{A13}$$

E_0 denotes the zero-point energy, m^* the reduced mass, and ω^* the (finite) phonon frequency. Up to this point the phonon force constant f^* has not been fixed; it and m^* set the scale for quantum phonon fluctuations. Note that Eq. (A10) represents an effective single-particle Hamiltonian, where the transfer integral is modified by the (real) band narrowing factor $\exp(-\Phi_{ls}^2)$ and an imaginary ω^*-dependent part. Moreover, the phonon frequency ω^* appears explicitly only in the hopping part of the Hamiltonian. An evaluation of the functional (A6) yields an upper bound for the true quantum-mechanical ground-state energy. Moreover, we have access to (at least) a second bound, since the EDCP (exact diagonalization of the electronic part of our model in combination with a classical treatment of the phonon degrees of freedom) can be interpreted in terms of a variational *Ansatz*.[23,49]

APPENDIX B: NUMERICAL METHOD FOR EXACT DIAGONALIZATION

We describe briefly here the EDCP method. Exact diagonalizations of the electronic part of the coupled electron-phonon Hamiltonian were performed using a Lanczos algorithm.[54] We used real-space basis states

$$|\{i_n\uparrow\},\{j_n\downarrow\}\rangle = c_{i_1\uparrow}^\dagger \cdots c_{i_{N_U}\uparrow}^\dagger \; c_{j_1\downarrow}^\dagger \cdots c_{j_{N_D}\downarrow}^\dagger \; |\,0\rangle ,$$

for up electrons at sites $i_1 < i_2 < \cdots < i_{N_U}$ and down electrons at sites $j_1 < j_2 < \cdots < j_{N_D}$, where the numbers N_U and N_D of up- and down-spin fermions are both fixed and $|\,0\rangle$ is the vacuum state. Apart from particle-number conservation, no other symmetries were used. Starting from an initial vector $|\psi_1\rangle$ (see below), an orthonormal basis was constructed by generating a sequence of states, $|\psi_1\rangle, |\psi_2\rangle, \ldots$, each expressed in terms of the real-space basis. Each state $|\psi_n\rangle$, $n \geq 2$, was generated by orthogonalizing $H|\psi_{n-1}\rangle$ to $|\psi_{n-1}\rangle$ and to $|\psi_{n-2}\rangle$ and normalizing. This procedure generates an orthonormal set and the Hamiltonian in this basis is tridiagonal.[54] Whenever generation of these basis vectors exceeded computer memory, we diagonalized the Hamiltonian in the limited basis and resumed the generation with the eigenvector corresponding to the lowest eigenvalue as the new trial ground-state wave function. The procedure was terminated whenever expanding the basis decreased our estimate of the ground state energy by less than some small amount—usually 10^{-5}.

Our initial ground-state trial wave function $|\psi_1\rangle$ was a random state, which is sure to have overlap with the true ground state for all sets of parameters. Convergence for a $\frac{3}{4}$-filled eight-site ring took minutes on a SUN workstation. Thereafter, using that ground state as the trial wave function for a set of Hamiltonian parameters reduced the computer time needed for convergence from minutes to seconds—provided, of course, that the change in parameters did not take one across a first-order phase transition (i.e., a discontinuous derivative of the ground-state energy with respect to Hamiltonian parameters due to the crossing of eigenvalues). Hence, phase boundaries could be mapped out quickly by running the diagonalization routine interactively—twice at once, with one job running on each side of the boundary. Each program would have to perform an expensive diagonalization starting from a random wave function only once; thereafter, one could vary parameters along the boundary smoothly for each program using the last ground state as a good guess for the point in parameter space.

Equilibrium displacements from uniform lattice spacing were determined using the self-consistency condition, $\partial\langle E_{\text{total}}\rangle/\partial\Delta_\ell = 0$, to relax the lattice distortion toward the minimum energy static solution (as was also done in the other adiabatic approaches, HFCP and PTCP). Adiabatic phonon modes could be calculated by stepping the lattice positions away from this minimum and calculating the dynamical matrix as a discrete second-difference of the total energy.

Once the estimates for the ground-state wave function $|\phi_0\rangle$ and energy E_0 were determined, optical-absorption spectra could be calculated. This is done by applying the current operator J to get an initial vector $|\tilde{\psi}_1\rangle$ for the Lanczos process, $J|\phi_0\rangle = A|\tilde{\psi}_1\rangle$ with $\langle\tilde{\psi}_1|\tilde{\psi}_1\rangle = 1$, yielding basis states $|\tilde{\psi}_n\rangle$ and a tridiagonal matrix $\tilde{H}_T$. Generating N_T entries to $\tilde{H}_T$ (the wave functions need not be stored) and truncating, estimates of the excited states are then given by $|\phi_k\rangle = B_{kn}|\tilde{\psi}_n\rangle$ where the B diagonalize $\tilde{H}_T$. The matrix elements needed in the golden rule for optical absorption are then

$$\langle\phi_k|J|\phi_0\rangle = \langle B_{kn}\tilde{\psi}_n|A\tilde{\psi}_1\rangle = B_{1k}^\dagger A \tag{B1}$$

and the energies needed are the eigenvalues of $\tilde{H}_T$ and E_0. Typically values of $N_T \lesssim 60$ were needed for the estimate of the optical absorption to stop changing at the 1% level.

APPENDIX C: FORMALISM FOR HARTREE-FOCK

Since several different levels of Hartree-Fock approximation are commonly used in the literature, we include here the specific formulation of HF used in this work. As stated in the Introduction, in HFCP we treat the lattice vibrations as classical variables. For the electronic part of the Hamiltonian, we replace

$$H_{e\text{-}e} = \sum_l U_l \, n_{l\uparrow} n_{l\downarrow} + \sum_l V n_l n_{l+1} , \tag{C1}$$

where $n_{ls} \equiv c_{l\uparrow}^\dagger c_{ls}$, with

$$H_{e\text{-}e}^{\mathrm{HF}} = \sum_{l,s} U_l \rho_{l,\bar{s}} n_{ls} - \sum_l U_l \rho_{l\uparrow}\rho_{l\downarrow} + \sum_l V(\rho_{l-1}+\rho_{l+1})n_l - \sum_l V\rho_l\rho_{l+1} , - \sum_{l,s} V(d_{ls}c_{ls}^\dagger c_{l+1s} + d_{ls}^\dagger c_{l+1s}^\dagger c_{ls}) + \sum_{l,s} V d_{ls}^\dagger d_{ls} \tag{C2}$$

where $\bar{s}$ denotes the opposite spin from s, $\rho_{ls} \equiv \langle 0|n_{ls}|0\rangle$ and $d_{ls} \equiv \langle 0|c_{l+1s}^\dagger c_{ls}|0\rangle$ (for $V \neq 0$) are determined self-consistently, and $|0\rangle$ is the electronic (many-particle, Slater) state under consideration. Keeping the last ("exchange") terms is important for spin-spin interactions. Even with $U = V = 0$, to get agreement of the spin-spin correlation functions with the EDCP results, terms of this type in that calculation are needed (otherwise $\langle S_i S_j \rangle = \langle S_i \rangle \langle S_j \rangle \equiv 0$). For the molecular dynamics, the minimum energy ρ and d for the instantaneous lattice configuration are found at each time step, whereas ρ, d, and Δ are relaxed in parallel when only the minimum energy configuration is sought. Further, when comparing the energy levels and total energy of the bare parameters with those of the HF effective $U = 0$ parameters, we added additional pressure, chemical potential, and constant terms to constrain these energies to be the same for both parameter sets in the uniform ground state:

$$\bar{H}_{e\text{-}e}^{\mathrm{HF}} = \sum_{l,s} \left(U_l \rho_{l,\bar{s}} - \langle U_l \rho_{l,\bar{s}}\rangle\right) n_{ls} - \sum_l \left(U_l \rho_{l\uparrow}\rho_{l\downarrow} - \langle U_l\rangle\langle\rho_{l\uparrow}\rangle\langle\rho_{l\downarrow}\rangle\right) + \sum_l V\left[(\rho_{l-1} - \langle\rho_{l-1}\rangle) + (\rho_{l+1} - \langle\rho_{l+1}\rangle)\right] n_l - \sum_l V\left(\rho_l\rho_{l+1} - \langle\rho_l\rangle^2\right) - \sum_{ls} V\left[(d_{ls} - \langle d_{ls}\rangle)c_{ls}^\dagger c_{l+1s} + (d_{ls}^\dagger - \langle d_{ls}^\dagger\rangle)c_{l+1s}^\dagger c_{ls}\right] + \sum_{l,s} V\left(d_{ls}d_{ls} - \langle d_{ls}\rangle^2\right), \tag{C3}$$

where $\langle \mathcal{O}_{ls}\rangle = \sum_l \mathcal{O}_{ls}/N$. We stress that we used completely unrestricted HF—arbitrary structure in real space was allowed for both the spin and charge densities. Numerical solutions were also checked for possible "symmetry trapping" by testing that initial conditions with a different symmetry converged to the same final configuration as, or a higher energy configuration than, solutions which began with the final symmetry. For the NiX parameters of Table III, a metastable CDW phase was found, though in the presence of defects, the CDW became unstable and the system converged to the SDW phase (plus defect).

[1] J. Tinka Gammel, A. Saxena, I. Batistić, A.R. Bishop, and S.R. Phillpot, preceding paper, Phys. Rev. B **45**, 6408 (1992).

[2] M.B. Robin and P. Day, in *Advances in Inorganic Chemistry and Radiochemistry*, edited by H.J. Emeleus (Academic, New York, 1967), Vol. 10, p. 247; P. Day, in *Low Dimensional Cooperative Phenomena*, edited by H.J. Keller (Plenum, New York, 1974), p. 191; H.J. Keller, in *Extended Linear Chain Compounds*, edited by J.S. Miller (Plenum, New York, 1982), Vol. 1, p. 357; R. J. H. Clark, in *Advances in Infrared and Raman Spectroscopy*, edited by R. J. H. Clark and R. E. Hester (Wiley, New York, 1984), Vol. 11, p. 95.

[3] See the several contributions on MX chains in the Proceedings of the International Conference on the Science and Technology of Synthetic Metals, ICSM, Tübingen, West Germany, 1990 [Synth. Metals **41-43** (1991)].

[4] K. Nasu, J. Phys. Soc. Jpn. **50**, 235 (1981); **52**, 3865 (1983); **53**, 302 (1984); **53**, 427 (1984); **54**, 1933 (1985); J. Lumin. **38**, 90 (1987); K. Nasu and Y. Toyozawa, J. Phys. Soc. Jpn. **51**, 2098 (1982); **51**, 3111 (1982); A. Mishima and K. Nasu, Synth. Metals **29**, F175 (1989); Phys. Rev. B **40**, 5593 (1989).

[5] Y. Ichinose, Solid State Commun. **50**, 137 (1984).

[6] Y. Onodera, J. Phys. Soc. Jpn. **56**, 250 (1987).

[7] D. Baeriswyl and A.R. Bishop, Phys. Scr. **T19**, 239 (1987); J. Phys. C **21**, 339 (1988).

[8] S. D. Conradson, M. A. Stroud, M. H. Zeitlow, B. I. Swanson, D. Baeriswyl, and A. R. Bishop, Solid State Commun. **65**, 723 (1988).

[9] R.C. Albers, Synth. Metals **29**, F169 (1989); R.C. Albers, M. Alouani, J.M. Wills, and M. Springborg, *ibid.* **41/43**, 2739 (1991).

[10] R. C. Albers, M. Alouani, J. M. Wills, and M. Springborg, Synth. Metals **41-43**, 2739 (1991); M. Alouani and R.C. Albers (unpublished).

[11] The unpublished *ab initio* calculations were performed variously by C. Boyle (private communication), R. L. Martin (private communication), and P. J. Hay (private communication).

[12] J. Tinka Gammel, R.J. Donohoe, A.R. Bishop, and B.I. Swanson, Phys. Rev. B **42**, 10 566 (1990).

[13] E.g., Proceedings of the IBM Europe Institute 1988 Workshop on High Temperature Superconductivity, Oberlech, Austria (August 1988), edited by K.A. Muller: [IBM J. Res. Dev. **33** (1989)].

[14] V.J. Emery, Phys. Rev. Lett. **58**, 2794 (1987); **65**, 1076 (1990).

[15] J.T. Gammel, I. Batistić, A.R. Bishop, E.Y. Loh, Jr., and S. Marianer, Physica B **163**, 458 (1990).

[16] J. E. Hirsch and F. Marsigilio, Phys. Rev. B **39**, 11 515 (1989).

[17] J. Hubbard and J. B. Torrance, Phys. Rev. Lett. **47**, 1750 (1981).

[18] In Hartree-Fock approximation the Hubbard terms (U_M, U_X, V) have the same (disproportionation) effect on

the band structure and lattice distortion as the on-site e-ph interaction (β_M, β_X). Both mechanisms—$V > U$ [e.g., C. M. Varma, Phys. Rev. Lett. **61**, 2713 (1988)] and on-site e-ph coupling [e.g., T. M. Rice and L. Sneddon, *ibid.* **47**, 689 (1981)]—have been proposed to drive the CDW in $Ba_{1-x}Pb_xBiO$ and both yield effective "negative U" models. Similar choices may exist in the MX chain compounds.

[19] S.M. Weber-Milbrodt (unpublished).

[20] P.W. Anderson, Phys. Rev. Lett. **34**, 953 (1975).

[21] A. Painelli and A. Girlando, Synth. Metals **29**, F181 (1989); A. Girlando and A. Painelli, Synth. Metals **42/43**, 2721 (1991).

[22] W. Schmidt and M. Schreiber, Z. Phys. B **62**, 423 (1986); J. Chem. Phys. **86**, 953 (1987); J. Lumin. **38**, 141 (1987).

[23] S. Weber and H. Büttner, Solid State Commun. **56**, 395 (1985).

[24] J. Tinka Gammel, S.M. Weber-Milbrodt, E.Y. Loh, Jr., and A.R. Bishop, Synth. Metals **29**, F161 (1989).

[25] J.T. Gammel, S.M. Weber-Milbrodt, A.R. Bishop, E.Y. Loh, S. Marianer, and J. Reichl, Synth. Metals **41/43**, 2755 (1989).

[26] I. Batistić, X. Z. Huang, and A. R. Bishop (unpublished).

[27] The importance of further neighbor terms has been recognized in studies of neutral-to-ionic phase transitions in the related charge-transfer salts [e.g., B. Horovitz and J. Solyom, Phys. Rev. B **35**, 7081 (1987)], where they can lead to excitonic effects.

[28] The simple expansion in e_0, given in Table I, only gives good agreement with the two-band model for large e_0. For a discussion of effective one-band models which appear to be valid for experimentally relevant parameters, see the discussion in Appendix B of paper I. Note that this implies that the deviation in charge, and hence the Hubbard U, are different between the one- and two-band models.

[29] K. Toriumi *et al.*, Mol. Cryst. Liq. Cryst. **181**, 333 (1990).

[30] I. Batistić, A. Saxena, A. R. Bishop, and M. Alouani (unpublished).

[31] M. Springborg and O.K. Anderson, J. Chem. Phys. **87**, 7125 (1987).

[32] H. Röder, J.T. Gammel, and A.R. Bishop (unpublished).

[33] E. Pytte, Phys. Rev. B **10**, 4637 (1974).

[34] S. Kivelson, W.P. Su, J.R. Schrieffer, and A.J. Heeger, Phys. Rev. Lett. **58**, 1899 (1987).

[35] A. Zawadowski, Phys. Rev. B **39**, 4682 (1989); Solid State Commun. **70**, 439 (1989).

[36] K. Nasu, Phys. Rev. B **42**, 6076 (1990).

[37] H. Toftlund and O. Simonsen, Inorg. Chem. **23**, 4261 (1984); K. Toriumi, Y. Wada, T. Mitani, S. Bandow, M. Yamashita, and Y. Fujii, J. Am. Chem. Soc. **111**, 2341 (1989).

[38] M. Yamashita, Y. Nonaka, S. Kida, Y. Hamaue, and R. Aoki, Inorg. Chim. Acta **52**, 43 (1981); D.A. Cooper, S.J. Higgins, and W. Levason, J. Chem. Soc. Dalton Trans. **1983**, 2131 (1983).

[39] R.E. Peierls, *Quantum Theory of Solids* (Clarendon, Oxford, 1955), p. 108.

[40] I. Batistić, J.T. Gammel, and A.R. Bishop, Synth. Metals **41/43**, 2727 (1991); I. Batistić, J.T. Gammel, and A.R. Bishop, Phys. Rev. B **44**, 13 228 (1991).

[41] S. Aubry, P. Quemerais, and J.-L. Raimbault, in *Proceedings of the Third European Conference on Low Dimensional Superconductors, Dubrovnik, Yugoslavia, 1989*, edited by S. Barišić [Fisica **21**, 98 (1989)]; *ibid.* **21**, 106 (1989); S. Aubry, G. Abramovici, D. Feinberg, P. Quemerais, and J.-L. Raimbault, in *Proceedings of the Sixth Interdisciplinary Workshop on Nonlinear Coherent Structures in Physics, Mechanics, and Biological Systems, Montpellier, France, 1989*, Lecture Notes in Physics Vol. 353 (Springer, Berlin, 1985), p. 103.

[42] cf., E. Tosatti and L. Yu, Physica C **153**, 1253 (1988).

[43] J. Tinka Gammel, A. Saxena, and A.R. Bishop, Synth. Metals **41/43**, 2761 (1991).

[44] S. Marianer (unpublished); J. Reichl (unpublished); H. Röder (unpublished).

[45] S. Kurita, M. Haruki, and K. Miyagawa, J. Phys. Soc. Jpn. **57**, 1789 (1988); S. Kurita and M. Haruki, Synth. Metals **29**, F129 (1989); L. Degiorgi, P. Wachter, M. Haruki, and S. Kurita, *ibid.* **29**, F137 (1989).

[46] Y. Wada, T. Mitani, M. Yamashita, and T. Koda, J. Phys. Soc. Jpn. **54**, 3143 (1985).

[47] M. Haruki and P. Wachter, Phys. Rev. B **43**, 6273 (1991).

[48] E.Y. Loh and D.K. Campbell, Synth. Metals **27**, A499 (1988).

[49] S. Weber and H. Büttner, J. Phys. C **17**, L337 (1984); S. Weber, thesis (Dissertation), University of Bayreuth, 1985; S. M. Weber-Milbrodt and H. Büttner (unpublished).

[50] M. C. Gutzwiller, Phys. Rev. Lett. **10**, 159 (1963); Phys. Rev. **134**, A923 (1964); **137**, A1726 (1965).

[51] S.M. Weber-Milbrodt and D.K. Campbell (unpublished); S.M. Weber-Milbrodt, Synth. Metals **43**, 3571 (1991).

[52] D. Baeriswyl and K. Maki, Phys. Rev. B **31**, 6633 (1985).

[53] S.M. Weber-Milbrodt, Synth. Metals **27**, A509 (1988).

[54] See, e.g., the section on Lanczos diagonalization in S. Pissanetsky, *Sparse Matrix Technology* (Academic, London, 1984).

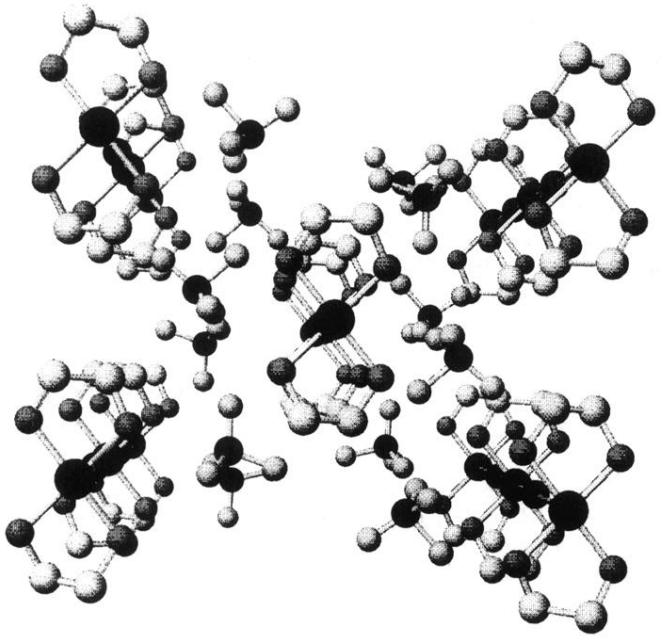

FIG. 1. X-ray diffraction crystal structure of the PtX material $[Pt(en)_2][Pt(en)Cl_2]\cdot(ClO_4)_4$, looking down the chains. There are two equivalent $(ClO_4)^-$ rotations and we have randomly chosen one. The atoms are, from darkest to lightest, Cl, Pt, N, O, and C.